THE JOURNAL OF PHYSICAL CHEMISTRY C

Article

Cite This: J. Phys. Chem. C 2019, 123, 8447−8462

pubs.acs.org/JPCC

# Hydrogen Chemisorption Isotherms on Platinum Particles at Catalytic Temperatures: Langmuir and Two-Dimensional Gas Models Revisited

Mónica García-Diéguez,[†] David D. Hibbitts,*[,†,‡] and Enrique Iglesia*[,†,§]

[†]Department of Chemical and Biomolecular Engineering, University of California, Berkeley, California 94720, United States

[‡]Department of Chemical Engineering, University of Florida, Gainesville, Florida 32601, United States

[§]Division of Chemical Sciences, E. O. Lawrence Berkeley National Laboratory, Berkeley, California 94720, United States

Supporting Information



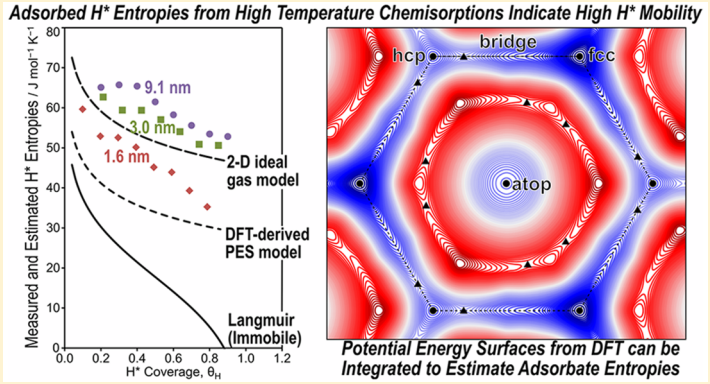


**ABSTRACT:** Density functional theory (DFT) and dihydrogen chemisorption uptakes at temperatures relevant to catalysis are used to determine and interpret adsorption enthalpies and entropies over a broad range of chemisorbed hydrogen (H*) coverages (0.1 ML to saturation) on Pt nanoparticles (1.6, 3.0, and 9.1 nm mean diameters) and Pt(111) surfaces. Heats of adsorption decrease by 30 kJ mol$^{-1}$ as $H_2$ coverage increases from nearly bare (0.1 ML) to saturated (∼1 ML) surfaces, because of the preferential saturation of low-coordination surface atoms by H* at low coverages. Such surface nonuniformity also leads to stronger binding on small Pt particles at all coverages (e.g., 47 kJ mol$^{-1}$ on 1.6 nm, 40 kJ mol$^{-1}$ on 3.0 nm, and 37 kJ mol$^{-1}$ on 9.1 nm particles all at 0.5 ML), because their surfaces expose a larger fraction of low-coordination atoms. As H* approaches monolayer coverages, H*−H* repulsion leads to a sharp decrease in binding energies on all Pt particles. Measured H* entropies decrease with increasing H* coverage and decreasing particle size, but their values (35−65 J mol$^{-1}$ K$^{-1}$) are much larger than for immobile H* species at all coverages and particle sizes. Two-dimensional gas models in which mobile H* adsorbates move rapidly across uniform (ideal), excluded-area, or DFT-predicted nonuniform potential energy surfaces all give H* entropies ≥30 J mol$^{-1}$ K$^{-1}$, qualitatively consistent with measured values. Larger H* entropies are predicted for uniform (ideal) PES while smaller H* entropies are predicted using nonuniform PES. DFT-derived barriers for H* diffusion between hcp and fcc 3-fold sites on Pt(111) surface are about 6 kJ mol$^{-1}$, a value similar to thermal energies ($kT$) at temperatures of catalytic relevance, consistent with fast diffusion in the time scale of adsorption−desorption events and isotherm measurements. Mobile adsorbate entropy models are therefore essential for accurate estimates of adsorbate coverages, particularly because vibrational frequencies analyzed by harmonic oscillator approximations lead to large underpredictions of entropies, resulting in DFT-predicted adsorption free energies that are too large to result in high coverages—even at conditions where H* is known to cover the surface. The nonuniformity of Pt surfaces, repulsion among coadsorbates, and high adsorbate mobility starkly contrast with the requirements for Langmuirian descriptions of binding and reactions at surfaces, despite the ubiquitous use and success in practice of the resulting equations in describing adsorption isotherms and reaction rates on surfaces. Such fortuitous agreement is a likely consequence of the versatility of their functional form, taken together with the limited range in pressure and temperature in adsorption and kinetic measurements. The adsorption and kinetic constants derived from such data, however, would differ significantly from theoretical estimates that rigorously account for surface coordination, adsorbate mobility, and coadsorbate repulsion.

## 1. INTRODUCTION

Heterogeneous catalysis involves the chemisorption and reactions of bound intermediates.[1,2] The enthalpies and entropies of such chemisorbed species and of the transition

Special Issue: Hans-Joachim Freund and Joachim Sauer Festschrift

Received: November 9, 2018
Revised: January 6, 2019
Published: January 31, 2019




DOI: 10.1021/acs.jpcc.8b10877
J. Phys. Chem. C 2019, 123, 8447−8462

states that mediate their interconversions provide the thermodynamic formalism that permits rigorous interpretations of reaction rates and selectivities. The chemisorption of specific reactants and of probe molecules are also used to titrate—and thus to count and characterize—binding sites at catalytic surfaces.[1,2] Chemisorbed H atoms (H*), formed via $H_2$ dissociation, are attractive titrants for metal catalysts because their binding is relatively strong but yet reversible and give hydrogen-to-surface-metal ($H:M_{surf}$) stoichiometries that depend on surface structure and cluster size[3] to a lesser extent than other titrants (e.g., CO*, O*). Dihydrogen is also a ubiquitous reactant in the hydrogenation or hydrogenolysis of many substrates,[1,2,4−6] such as alkanes,[7−15] alkenes,[16−18] CO,[19−22] arenes,[23] organosulfur compounds[24,25] and $NO_x$.[26,27] Accurate thermodynamic data for $H_2$ chemisorption at temperatures and coverages relevant to catalysis are essential to probe the nature of catalytic surfaces, the relevance and accuracy of thermodynamic adsorption parameters derived from mechanistic interpretations of kinetic data for relevant reactions, and the adequacy of Langmuirian models for molecular binding and surface reactions.

Matters of mobility and binding energy at temperatures of catalytic practice are essential for rigorous kinetic treatments of chemical reactions, which often treat elementary steps as occurring on surfaces consisting of well-defined sites and which bind immobile chemisorbed species with energies and reactivities that are insensitive to coverage.[28] Such Langmuirian treatments of surfaces (and of catalytic reactions) have succeeded remarkably in describing how rates vary with reactant and product concentrations, despite their restrictive assumptions. Their success has led to a level of comfort with Langmuirian treatments that is seldom supported by more rigorous analyses. The effects of coverage have become a major topic of interest for studies of CO oxidation,[29−31] alkanes hydrogenolysis,[15] alkanol decarbonylation,[32] and CO hydrogenation[22,33] reactions on CO*-saturated surfaces, as well as for $CH_4-O_2$ and $NO-O_2$ reactions on O*-covered surfaces,[34,35] while the topic of adsorbate mobility and the consequence on Langmuirian models has typically raised fewer significant concerns.

$H_2$ uptakes at near ambient temperatures (298−400 K) are often used to determine the fraction of the metal atoms in a sample that are exposed at surfaces (dispersion) using *ad hoc* distinctions among coexisting species bound more or less strongly. These protocols are guided by the reversibility of adsorption events during evacuation at a given temperature for a specific period of time. The metal dispersions are then reported based on irreversible $H_2$ uptakes using a saturation $H:M_{surf}$ stoichiometry of unity, which is likely to be inaccurate, and especially so for small metal particles (<4 nm).[3] The frequent agreement between mean diameters estimated from these uptakes and from surface-averaged diameters derived from transmission electron microscopy (TEM) histograms is typically used as the arbiter of accuracy; yet, the choice of adsorption temperature and evacuation pressure or time remains arbitrary, in view of M−H bond strengths that vary with surface structure, adsorbate coverage, and metal identity.

$H_2$ adsorption enthalpies ($\Delta H_{ads,H_2}$) at near-ambient temperatures and low coverages have been widely reported on Pt single crystals (Pt(100),[36,37] Pt(110),[38] Pt(111),[39−41] and Pt(997)[42]), unsupported Pt,[43−46] and supported Pt particles[43,47,48] using calorimetry,[43,44,47,48] adsorption isotherms,[42,44,45] and work function measurements.[41] These data, however, are typically acquired at temperatures and coverages well below those prevalent in the practice of catalysis. Adsorption entropies ($\Delta S_{ads,H_2}$) are seldom reported at these relevant temperatures (>400 K), rendering conclusions about the mobility of adsorbed species and about the fidelity of the interpretive adsorption models uncertain and possibly inaccurate. Density functional theory (DFT) has been used to examine adsorption potential energies ($\Delta E_{ads,H_2}$) of $H_2$ on Pt surfaces, most commonly on low-index Pt(100) and Pt(111) surfaces and on Pt ensembles (2−147 Pt atoms).[49−62] Vibrational frequency calculations are sometimes used, together with $\Delta E_{ads,H_2}$ values, to estimate $\Delta H_{ads,H_2}$ and $\Delta S_{ads,H_2}$ values for $H_2$ chemisorption above 0 K, which can be used, in turn, to calculate adsorption free energies ($\Delta G_{ads,H_2}$) and $H_2$ adsorption equilibrium constants ($K_{H_2}$) at these temperatures.

Recent studies have demonstrated the use of hindered translator models of adsorbate motion[63−65] which model 2-dimensional potentials as sinusoidal variations rather than the standard harmonic oscillator approximation. These models result in larger entropies of adsorbed species as a function of the diffusional barriers (the variation in the sinusoidal functions) associated with translation between surface binding sites. Subsequent work[66] examining H* and other adsorbates on Au and Pt(100) surfaces describe the potential energies of the adsorbates using DFT-calculated potential energy surfaces which can be treated through quantum and semiclassical methods to calculate adsorbate free energies and entropies. A similar approach was also examined for CO oxidation on Pt(111) surfaces.[67] These previous descriptions demonstrate that entropies of adsorbed intermediates far exceed values assumed from harmonic oscillator treatments.

Here, we report $H_2$ chemisorption isotherms at temperatures relevant to catalytic practice (523−673 K) on Pt particles dispersed on $Al_2O_3$ or $SiO_2$ (9.1, 3.0, and 1.6 nm mean diameter) and DFT-calculated potential energy surface (PES) of H* Pt(111) surfaces at various coverages. These data show that $\Delta H_{ads,H_2}$ values become less negative (i.e., H* binds more weakly) as coverage increases, even at coverages well below a monolayer, because of the combined effects of surface nonuniformity and of through-surface repulsion among H* as their coverage increases; these H* species show differential adsorption entropies ($S_{H^*} > 30$ J mol$^{-1}$ K$^{-1}$ at all coverages, 593 K) that are inconsistent with immobile adsorption models of the H* adlayer ($S_{H^*} \sim 15$ J mol$^{-1}$ K$^{-1}$ at 593 K). Mobile adsorbate models, in contrast, predict differential adsorption entropies larger than 30 J mol$^{-1}$ K$^{-1}$ (593 K) and much closer to measured values. These models can be used with a uniform PES (two-dimensional ideal gas), a surface with excluded area from coadsorbed H* (similar to a Volmer gas), or with a PES derived from DFT on the Pt(111) surface, which is the prevalent surface of large particles.

Differential enthalpies and entropies of adsorption are used here as probes of the intrinsic nonuniformity of cluster surfaces and of the effects of coverage through coadsorbate interactions. These findings confirm and reinforce the conceptual and practical concerns about Langmuirian treatments of adsorption and surface reactions and shed light on how more accurate adsorption and surface reaction models can be constructed to account for surface nonuniformity, coadsorbate interactions, and adsorbate mobility.



DOI: 10.1021/acs.jpcc.8b10877
J. Phys. Chem. C 2019, 123, 8447−8462

## 2. EXPERIMENTAL METHODS

**2.1. Catalysts Synthesis.** $Pt/Al_2O_3$ (1.6 wt %) was prepared by incipient wetness impregnation of $\gamma$-$Al_2O_3$ (Sasol North America Inc., Lot No.C1643, 193 $m^2$ $g^{-1}$, 0.57 $cm^3$ $g^{-1}$ pore volume), previously treated in flowing dry air (Praxair, 99.99%, 0.8 $cm^3$ $g^{-1}$ $s^{-1}$) at 923 K (0.083 K $s^{-1}$, held for 3 h), with an aqueous solution of $H_2PtCl_6(H_2O)_6$ (Aldrich, CAS 16941-12-1; 8% by wt. in $H_2O$; 0.43 mL per gram of $Al_2O_3$). The impregnated supports were kept overnight at 373 K in stagnant ambient air. The resulting material was divided into two portions, which were treated in flowing dry air (Praxair, 99.99%, 0.8 $cm^3$ $g^{-1}$ $s^{-1}$) at either 923 or 998 K by heating at 0.083 K $s^{-1}$ and holding for 3 h to obtain samples with different Pt dispersion and cluster size. Samples were cooled to ambient temperature in flowing dry air, flushed with He, and exposed to flowing $H_2$ (10% in He, Praxair, 1.67 $cm^3$ $g^{-1}$ $s^{-1}$) by heating to 773 at 0.033 K $s^{-1}$, holding for 3 h and subsequently cooling to 523 K. Samples were then exposed to flowing He (Praxair UHP grade, 0.8 $cm^3$ $g^{-1}$ $s^{-1}$), cooled to ambient temperature and passivated with 0.5% $O_2$–He (Praxair certified standard, 0.8 $cm^3$ $g^{-1}$ $s^{-1}$) at ambient temperature for 1 h before exposing them to ambient air.

$Pt/SiO_2$ (1.0 wt %) was prepared using electrostatic adsorption methods,[68] in which negatively charged $SiO_2$ at the prevalent solution pH strongly interacts with cationic Pt precursors to form highly dispersed bound precursors that lead to small Pt domains upon thermal treatment. $SiO_2$ (20 g, Davisil 646, Sigma-Aldrich) was suspended in deionized $H_2O$ (200 $cm^3$) and the pH increased to 9 by adding $NH_4OH$ (14 M). The Pt precursor ($Pt(NH_3)_4(NO_3)_2$, Sigma; 0.4 g) was then added and the mixture was stirred for 1 h at ambient temperature. The suspension was filtered and treated at 373 K for 6 h in flowing He (Praxair UHP grade, 0.8 $cm^3$ $g^{-1}$ $s^{-1}$) and powders were then heated to 723 K (at 0.033 K $s^{-1}$) in a flowing mixture of 50% $H_2$ in He (Praxair UHP grade, 0.8 $cm^3$ $g^{-1}$ $s^{-1}$), held at 723 K for 3 h, and cooled to ambient temperature in this flowing mixture. The samples were passivated by contact with a flowing 0.5% $O_2$–He mixture (Praxair certified standard, 0.8 $cm^3$ $g^{-1}$ $s^{-1}$) for 1 h before exposure to ambient air.

**2.2. Transmission Electron Microscopy and $H_2$ Chemisorption Measurements.** $H_2$ adsorption isotherms were determined from $H_2$ uptakes measured in a volumetric apparatus at 473–673 K. The apparatus consists of a quartz tube (reactor cell; 9–10 $cm^3$) with a fritted sample holder, a thermocouple (K-type) in contact with the outer tube wall, and a stainless steel dosing chamber (11.9 $cm^3$). Leak rates in these systems were $<3 \times 10^{-9}$ mol $h^{-1}$ at ambient temperature and $<6 \times 10^{-9}$ mol $h^{-1}$ at 973 K. Samples (~1 g) were placed in the adsorption cell and treated at 723 K in flowing $H_2$ (1.33 $cm^3$ $s^{-1}$, Praxair UHP grade, 0.083 K $s^{-1}$ heating rate) for 1 h and then evacuated for 2 h using a turbomolecular pumping system (TMU 071 P, Pfeiffer) and a rotary vane pump (Varian DS 302) capable of a dynamic vacuum $<10^{-6}$ Pa. After evacuation, samples were cooled to the adsorption temperature and $H_2$ uptakes were measured by increasing the $H_2$ pressure from 0.1 to 20 kPa using sequential injection of $H_2$ pulses ($H_2$ Praxair UHP grade) at 0.9–3.6 ks intervals to allow full equilibration. Pressures were measured with a dual-range transducer (0.1–13 kPa and 0.1–133 kPa; MKS Baratron, type D28B; 0.25% accuracy; resolution of 0.001% of full scale). The effective cell volume was determined at each temperature using He as an inert gas.

The diameter of the Pt particles inferred from saturation adsorption during $H_2$ chemisorption isotherms were compared to surface-averaged mean diameters from transmission electron microscopy (TEM):

$$\bar{D}_{TEM} = \frac{\sum n_i d_i^3}{\sum n_i d_i^2} \quad (1)$$

Here $n_i$ is the number of crystallites having a diameter $d_i$.[69] Transmission electron micrographs were obtained with a FEI Tecnai 12 transmission electron microscope at 120 kV. The cluster size uniformity of the Pt particles is reported as the dispersity index (DI):[70]

$$\mathrm{DI} = \frac{\sum n_i \sum n_i d_i^4}{\sum n_i d_i \sum n_i d_i^3} \quad (2)$$

**2.3. Computational Methods.** Periodic plane-wave DFT calculations were performed using the Vienna *ab initio* simulation package (VASP)[71−74] to estimate adsorption energies and PES for H* species on Pt(111). Plane-waves were constructed using projector augmented-wave (PAW) potentials with an energy cutoff of 400 eV.[75,76] The revised Perdew–Burke–Ernzerhof (RPBE) and Perdew–Wang 91 (PW-91) forms of the generalized gradient approximation (GGA) were both used to determine exchange and correlation energies.[77−80] Dispersion corrections, when included, were performed using the DFT-D3 method with Becke–Johnson damping.[81,82] Wave functions for all calculations were converged to within $10^{-8}$ eV and the sampling of the Brillouin zone (*k*-point mesh) was increased for small unit cell sizes in Pt surface model (Table 1); a 1 × 1 × 1 mesh was used for calculations of gas-phase $H_2$. Forces were computed using a fast Fourier transform (FFT) grid with a cutoff equal to two times the planewave cutoff; all structures were relaxed until forces on unconstrained atoms were <0.01 eV $Å^{-1}$ during optimizations.

Pt(111) surfaces were chosen because the (111) surface is the prevalent exposed facet for Pt particles larger than 2 nm.[83] The experimental lattice constant for bulk Pt metal (0.39239 nm)[84] was used to construct this surface. Pt(111) surfaces were modeled using a range of unit cell sizes (from 1 × 1 to 4 × 4) to vary the H* coverage in a systematic manner as illustrated in Table 1. The slab models contained four layers in the direction normal to the (111) surface; the bottom two layers were held fixed in their bulk crystallographic locations and the top two layers were allowed to relax.

**Table 1. Pt(111) Unit Cell Sizes and H* Coverages Examined**

| unit cell | H* | $\theta_H$, ML | *k*-point mesh |
|---|---|---|---|
| 1 × 1 | 1 | 1 | 24 × 24 × 1 |
| 1 × 2 | 1 | 1/2 | 24 × 12 × 1 |
| 1 × 3 | 1 | 1/3 | 24 × 8 × 1 |
| 2 × 2 | 1 | 1/4 | 12 × 12 × 1 |
| 2 × 3 | 1 | 1/6 | 12 × 8 × 1 |
| 3 × 3 | 1 | 1/9 | 8 × 8 × 1 |
| 3 × 4 | 1 | 1/12 | 8 × 6 × 1 |
| 4 × 4 | 1 | 1/16 | 6 × 6 × 1 |
| 4 × 4 | 16 | 1 | 6 × 6 × 1 |

*2.3.1. Harmonic Oscillator Treatment of Vibrational Modes.* The vibrational frequencies for chemisorbed H* species on Pt(111) surfaces were calculated from their Hessian matrix, which was obtained using finite difference methods with four displacements in each Cartesian coordinate for all H* atoms. All metal atoms were constrained during these frequency



DOI: 10.1021/acs.jpcc.8b10877
J. Phys. Chem. C 2019, 123, 8447–8462

calculations; thus, changes in metal−metal (M−M) bond vibrations upon H* adsorption were not included in the general analysis to reduce computational requirements. The inclusion of these M−M bond vibrations led to changes <3 kJ $mol^{-1}$ in adsorption free energies and <5 J $mol^{-1}$ $K^{-1}$ in adsorption entropies (at 593 K on a 2 × 2 Pt(111) surface with 1 ML H* in 3-fold fcc binding mode). Frequency calculations were used to determine zero-point vibrational energies (ZPVE), vibrational enthalpies ($H_v$), entropies ($S_v$) and free energies ($G_v$):[85]

$$\mathrm{ZPVE} = \sum_i \left(\frac{1}{2}\nu_i h\right) \tag{3}$$

$$H_{vib} = \sum_i \left(\frac{\nu_i h e^{-\nu_i h/kT}}{1 - e^{-\nu_i h/kT}}\right) \tag{4}$$

$$S_{vib} = \sum_i \left(\frac{1}{T}\frac{\nu_i h e^{-\nu_i h/kT}}{1 - e^{-\nu_i h/kT}} - k \ln \frac{1}{1 - e^{-\nu_i h/kT}}\right) \tag{5}$$

$$G_{vib} = \sum_i \left(-kT \ln \frac{1}{1 - e^{-\nu_i h/kT}}\right) \tag{6}$$

from vibrational frequencies ($\nu_i$) for $H_2$(g) and H*. For gaseous $H_2$, translational and rotational enthalpies and free energies were computed from statistical mechanics (Section S1 in the Supporting Information). The total molar differential entropy for immobile H* must include the configurational entropy ($S_{H^*,conf}$) and vibrational entropy in all three directions ($S^{xyz}_{H^*,vib}$) as given by

$$S_{H^*,\mathrm{immobile}} = S_{H^*,\mathrm{conf}} + S^{xyz}_{H^*,\mathrm{vib}} \tag{7}$$

These entropies (and analogous enthalpy and free energy terms) can be used to calculate adsorption enthalpies, entropies, and free energies.

*2.3.2. Generation and Integration of the PES to Calculate Adsorption Enthalpies and Entropies.* H* atoms on a Pt(111) surface have three accessible degrees of freedom: lateral translations along the *xy* plane defined by the surface and one translational mode normal to the surface (*z*). Extended motion normal to the surface, however, will cause M−H bond cleavage and H* desorption as a radical, a step with a very large barrier, restricting this normal mode to a vibration; its frequency was calculated by constraining the H* at its *x* and *y* positions. These frequencies were used to calculate zero-point corrections to the potential energies ($\mathrm{ZPVE}_z$) using harmonic oscillator approximations. Frequencies normal to the (111) surface were very large (>1000 $cm^{-1}$ at all H* positions), consistent with significant barriers for extended motion and with the requirements for the harmonic oscillator approximation. This treatment of the *z*-coordinate using vibrational frequencies decreases the dimensionality of the PES for H* species. The two-dimensional PES was then calculated by sampling unique locations of H* on the Pt(111) surface and constraining H* atoms in the *x* and *y* dimensions while relaxing their *z*-coordinates during optimization. The potential energies ($E_0$) obtained were combined with $\mathrm{ZPVE}_z$ values to give two-dimensional $E_0$ values:

$$E_0(x, y) = E_0 + ZPVE_z \tag{8}$$

to obtain a PES ($E_0(x,y)$). This treatment is similar to that previously described for adsorbates on (100) surfaces[66] and CO* on Pt(111).[67]

This PES can then be used to calculate differential translational free energies ($G^{xy}_{H^*,PES}$) and entropies ($S^{xy}_{H^*,PES}$) using a semiclassical approach as described in Section S2 of the Supporting Information:[86,87]

$$G^{xy}_{H^*,\mathrm{PES}} = -RT\left[\ln\left(\left(\frac{1}{\Lambda_{th}^2}\right)\frac{1}{\theta_H}\iint e^{(-E(x,y)/kT)}\,dx\,dy\right)\right] \tag{9}$$

$$S^{xy}_{H^*,\mathrm{PES}} = R\left[\ln\left(\left(\frac{1}{\Lambda_{th}^2}\right)\frac{1}{\theta_H}\iint e^{(-E(x,y)/kT)}\,dx\,dy\right) + \frac{\iint \frac{E(x,y)}{kT} e^{(-E(x,y)/kT)}dx\,dy}{\iint e^{(-E(x,y)/kT)}\,dx\,dy} + 1\right] \tag{10}$$

where $\Lambda_{th}$ is the thermal de Broglie wavelength:

$$\Lambda_{th} = \frac{h}{(2\pi mkT)^{1/2}} \tag{11}$$

The $E(x,y)$ in eqs 9−10 is a PES normalized by the minimum potential energy throughout the surface ($E_{min}$):

$$E(x, y) = E_0(x, y) - E_{\min} \tag{12}$$

where $E_0(x,y)$ is given by eq 8 above. The density of H* is represented in eqs 9−10 by $\theta_H$, which is the H* density normalized by the density of surface-metal atoms:

$$\theta_H = \frac{[H^*]}{[Pt_{surf}]} \tag{13}$$

this pseudocoverage makes no assumptions about the nature of binding sites and is not limited by 1 ML as assumed by a classic Langmuirian surface model. eqs 9 and 10 can be rewritten, for convenience, in terms of an effective area term ($\alpha_{PES}$)

$$\alpha_{PES} = \iint e^{(-E(x,y)/kT)}\,dx\,dy \tag{14}$$

and a term reflecting the degeneracy of the PES ($\beta_{PES}$)

$$\beta_{PES} = \iint \frac{E(x, y)}{kT} e^{(-E(x,y)/kT)}\,dx\,dy \tag{15}$$

to give the following:

$$G^{xy}_{H^*,\mathrm{PES}} = -RT \ln\left(\frac{\alpha_{PES}}{\Lambda_{th}^2\theta}\right) \tag{16}$$

$$S^{xy}_{H^*,\mathrm{PES}} = R\left[\ln\left(\frac{\alpha_{PES}}{\Lambda_{th}^2\theta}\right) + \frac{\beta_{PES}}{\alpha_{PES}} + 1\right] \tag{17}$$

A two-dimensional ideal gas would yield a "flat" PES such that the relative energy, $E(x,y)$, would be 0 at all points. For such a surface, the effective area term ($\alpha_{PES}$) would be the area occupied by each metal atom ($\alpha_0$) and $\beta_{PES}$ would be 0, thus giving differential molar entropies as

$$S^{xy}_{H^*,\mathrm{ideal}} = R\left[\ln\left(\frac{\alpha_0}{\Lambda_{th}^2\theta}\right) + 1\right] \tag{18}$$

as shown in previous work.[87] We can also introduce an area-excluded model, in which coadsorbed H* occlude space (similar to a Volmer gas model), but which retains a flat PES ($E(x,y) = 0$



DOI: 10.1021/acs.jpcc.8b10877
J. Phys. Chem. C 2019, 123, 8447−8462

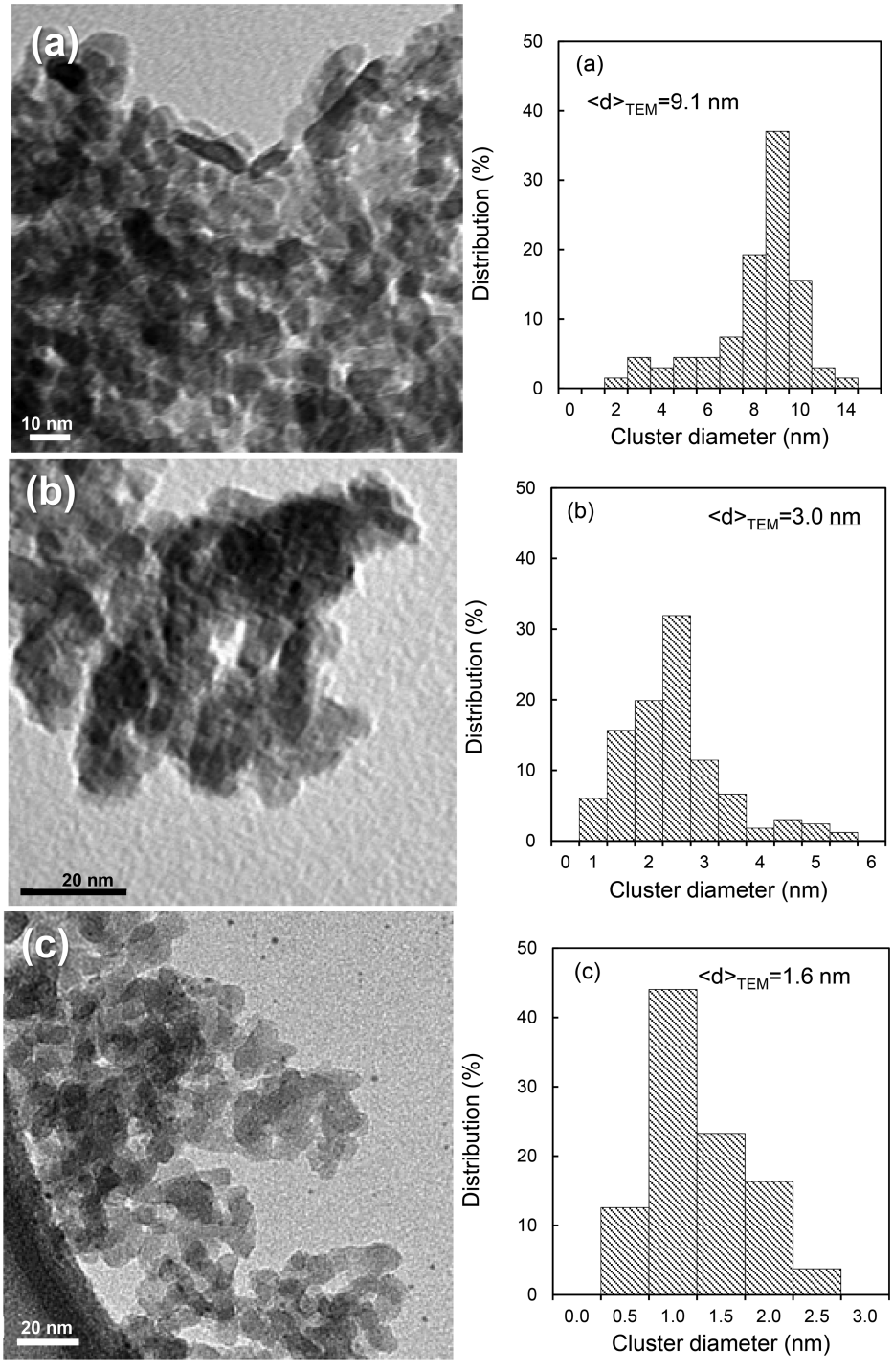


**Figure 1.** TEM images and Pt cluster size distributions for 1.6 wt % $Pt/Al_2O_3$ and 1 wt % $Pt/SiO_2$ samples (9.1 nm (a), 3.0 nm (b) and 1.6 nm (c) mean cluster size). Surface-area-weighted cluster diameters, $\langle d \rangle_{TEM}$ (eq 1, $n > 200$).

except within the excluded area, where $E(x,y)$ is infinite). This excluded area model gives a differential molar entropy as (derived in section S2, eqs S27−S29, of the Supporting Information):

$$S^{xy}_{H^*,co-area} = R\left[\ln\left(\frac{\alpha_0 - \theta b}{\Lambda^2_{th}\theta}\right) + 1 - \frac{b}{\alpha_0 - \theta b}\right] \quad (19)$$

where $b$ is the area excluded by each adsorbed H* (taken as half $\alpha_0$ in this work because H* can coexist in two 3-fold sites per metal atom on the Pt(111) surface). As $b \to 0$, eq 19 becomes identical to eq 18, that of the ideal two-dimensional gas. The molar differential entropy for mobile H* must also include the entropy of vibrations normal to the surface ($S^z_{H^*,vib}$) as given by

$$S_{H^*} = S^{xy}_{H^*} + S^z_{H^*,vib} \quad (20)$$

These entropies (and the analogous free energy terms) can be used to calculate adsorption enthalpies and entropies for $H_2$ adsorption.

Deviations between a quantum-mechanical treatment of the PES and the semiclassical treatment presented here are only significant at subambient temperatures,[66] indicating the



DOI: 10.1021/acs.jpcc.8b10877
J. Phys. Chem. C 2019, 123, 8447−8462

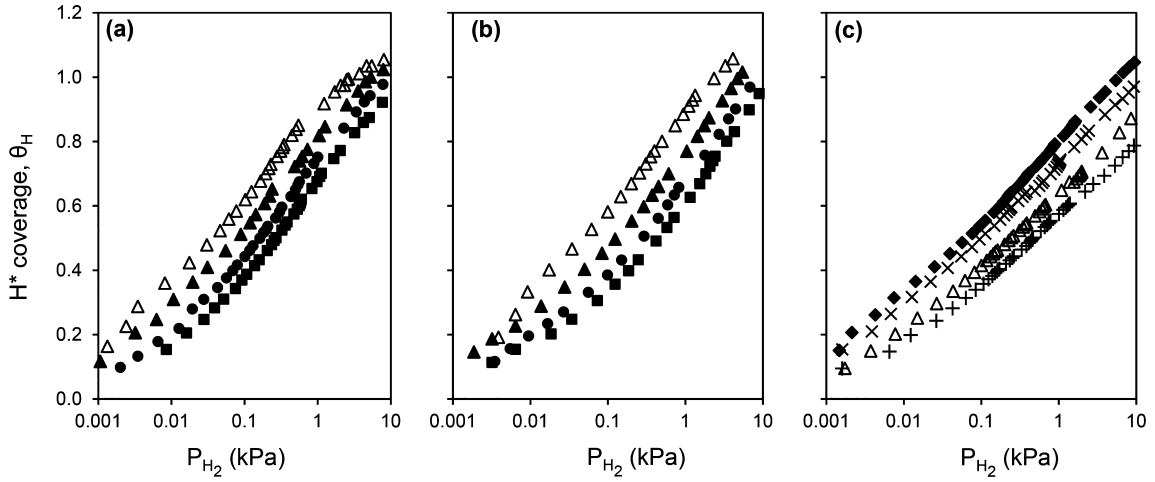


**Figure 2.** Adsorption isotherms for $H_2$ dissociative adsorption on Pt (1.6 wt % $Pt/Al_2O_3$ 9.1 nm (a) and 3.0 nm (b) mean cluster size; 1 wt % $Pt/SiO_2$ 1.6 nm mean cluster size (c)) at 673 K (■), 623 K (●), 573 K (▲), 548 (+), 523 K (△), 498 K (×), and 473 K (◆). Isotherms with a linear $H_2$ pressure scale are given in the Figure S1 of the Supporting Information.

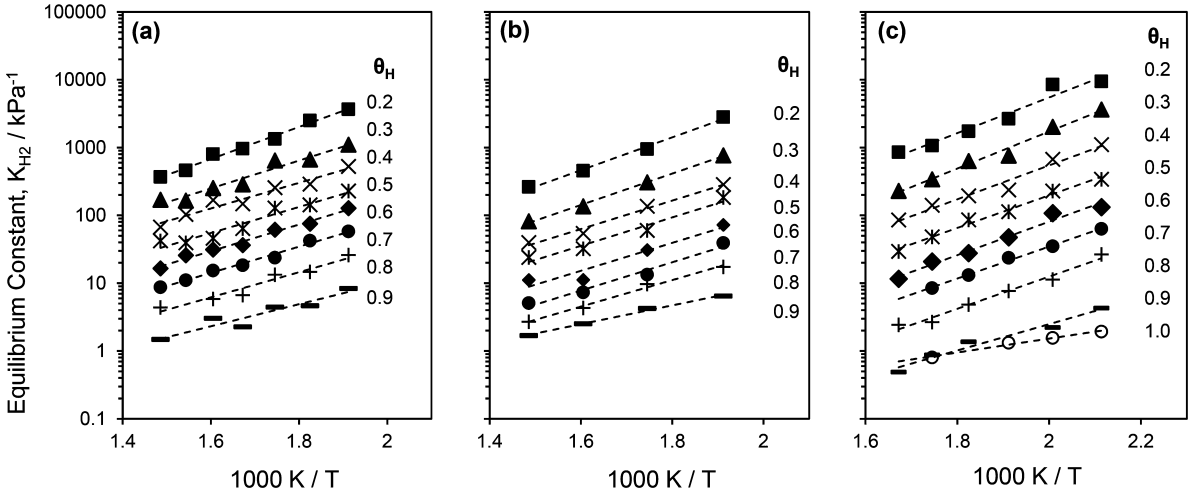


**Figure 3.** Equilibrium constant for hydrogen dissociative adsorption ($K_{H_2}$) on 1.6 wt % $Pt/Al_2O_3$ and 1 wt % $Pt/SiO_2$ samples (9.1 nm (a), 3.0 nm (b), and 1.6 nm (c) mean cluster size) at 0.2 (■), 0.3 (▲), 0.4 (×), 0.5 (∗), 0.6 (◆), 0.7 (●), 0.8 (+), 0.9 (−), and 1.0 (○) H* coverage ($\theta_H$).

approach used here is appropriate for these high temperature (473−673 K) isotherms.

## 3. RESULTS AND DISCUSSION

**3.1. $H_2$ Dissociative Adsorption on Pt Surfaces.** Different support and air-treatment temperatures led to materials with different mean Pt cluster diameter (Figure 1). Size effects on catalyst performance or $H_2$ uptake isotherms can be unequivocally interpreted only for samples with narrow size distributions, as given by a dispersity index (eq 2).[70] These indices were 1.3, 1.5, and 1.1 for Pt particles with 1.6, 3.0, and 9.1 nm surface-averaged mean diameters (eq 1), respectively, indicating that size distributions are quite narrow.[70,88] These TEM-derived particle sizes provide the number of surface-metal atoms ($Pt_{surf}$) used to normalize surface H* densities to give a fractional coverage ($\theta_H$, eq 13).

$H_2$ adsorption isotherms were obtained from measured $H_2$ uptakes on Pt particles (1.6 wt % $Pt/Al_2O_3$; 1 wt % $Pt/SiO_2$) with three different mean diameters (1.6, 3.0, and 9.1 nm) between 473 and 673 K. These $H_2$ adsorption isotherms are shown in Figure 2 (with the $H_2$ pressure shown on a logarithmic scale for visual clarity; the linear scale used in Figure S1 leads to the shape characteristic of the Langmuir adsorption isotherm). Fractional H* coverages ($\theta_H$, $H^*/Pt_{surf}$) are obtained by normalizing measured $H_2$ uptakes by the number of $Pt_{surf}$ atoms derived from TEM-derived surface-averaged diameters. These coverages do not assume any "saturation" behavior and thus need not be limited to 1 ML, given that undercoordinated metal atoms can bind more than one H*.[3]

The adsorption isotherms measured here (Figure 2) represent the dissociation of $H_2(g)$ to form two surface-bound H atoms that are bound to the metal surfaces without any indication, at this point, about the nature of the attachment or of the binding sites, of their uniformity, or of their total number:

$$H_2 \rightleftharpoons 2H^* \tag{21}$$

The surface is not treated as a template with a given number of uniform adsorption sites and therefore we do not include bare adsorption sites as reactants in the chemical stoichiometry of eq 21. The standard state adsorption free energy of $H_2$ is that for eq 21:

$$\Delta G^{\circ}_{H_2}(\theta_H, T) = 2G[H^*] - G[H_2] \tag{22}$$



DOI: 10.1021/acs.jpcc.8b10877
J. Phys. Chem. C 2019, 123, 8447−8462

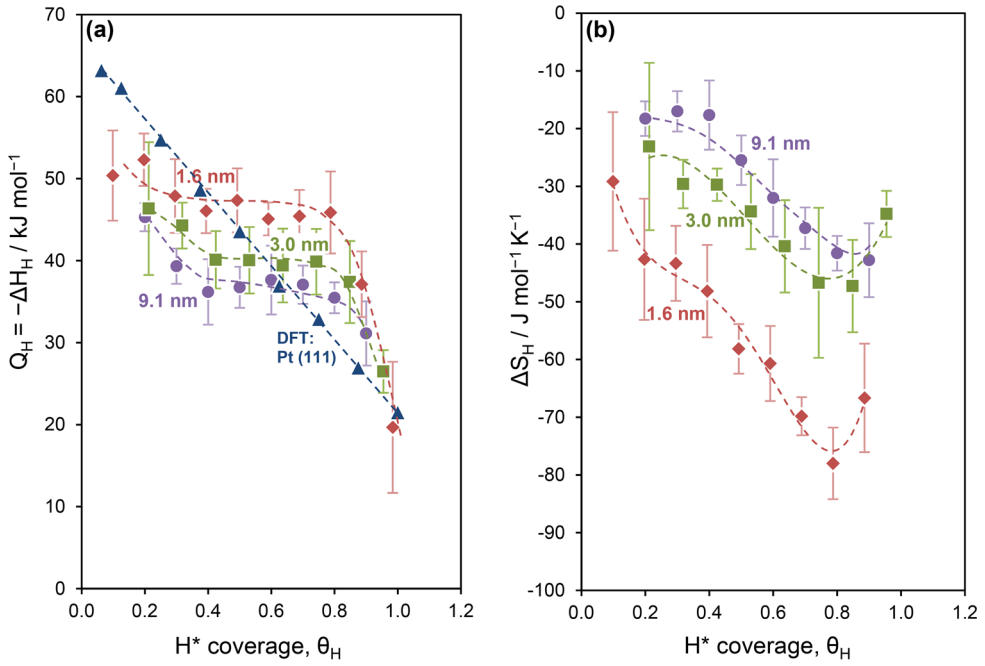


**Figure 4.** Changes in (a) enthalpy ($Q_{H_2} = -\Delta H_{H_2}^\circ$) and in (b) entropy per $H_2$ mol ($\Delta S_{H_2}^\circ$) upon $H_2$ adsorption on Pt (9.1 nm (●, purple), 3.0 nm (■, green), and 1.6 nm (◆, red) mean cluster size; 473−673 K) (dotted curves represent trends). DFT-derived adsorption enthalpies (RPBE) for H* bound to fcc sites on a Pt(111) surface are also shown (▲, blue) in part a. Error bars represent standard errors from Arrhenius fits shown in Figure 3.

where $G[H^*]$ and $G[H_2]$ represent the free energies of H* and $H_2$(g), respectively. This adsorption free energy ($\Delta G_{H_2}^\circ$) depends on the system temperature (T), the $H_2$ pressure (1 bar, standard state), and the density of surface-bound H* normalized by the density of surface-metal atoms ($\theta_H$, coverage, 1 ML, standard state). An equilibrium constant, $K_{H_2}$, can be defined based on the $H_2$ adsorption free energy at standard pressure (1 bar), $\Delta G_{H_2}^\circ$:

$$K_{H_2}(\theta_H, T) = \exp\left(\frac{-\Delta G_{H_2}^\circ(\theta_H, T)}{RT}\right) \quad (23)$$

This also depends on $\theta_H$ and $T$. At each increase in $H_2$ pressure during the isotherm measurements, the amount of $H_2$ disappearance is measured and described as a change in the coverage (eq 23) which is a normalized surface density. Thus, the resulting disappearance of $H_2$ into a product phase can be described, locally, as the derivative of the normalized surface density with respect to the local isotherm pressure:

$$K_{H_2}(\theta_H, T) = \frac{d\theta_H}{dP_{H_2}} \quad (24)$$

This describes the equilibrium relationship between H* and gas-phase $H_2$ and how it changes locally at each $\theta_H$ with $T$. Figure 3 shows that $K_{H_2}$ decreases with increasing $\theta_H$ and with increasing temperature on Pt particles with 1.6, 3.0, and 9.1 nm mean diameter dispersed on $Al_2O_3$ or $SiO_2$ (1.6 wt % $Pt/Al_2O_3$; 1 wt % $Pt/SiO_2$).

The position of equilibrium between H* and gas-phase $H_2$ depends on the standard state differential adsorption enthalpy ($\Delta H_{H_2}^\circ$) and entropy ($\Delta S_{H_2}^\circ$):

$$K_{H_2} = \exp\left(\frac{-\Delta G_{H_2}^\circ}{RT}\right) = \exp\left(\frac{-\Delta H_{H_2}^\circ}{RT} + \frac{\Delta S_{H_2}^\circ}{R}\right)$$

The temperature dependence of $K_{H_2}$ allows $\Delta G_{H_2}^\circ$ to be dissected into its individual enthalpy and entropy components at each H* coverage ($\theta_H$). The standard state differential heats of adsorption $Q_{H_2}$ ($-\Delta H_{H_2}^\circ$) and the standard state adsorption entropies ($\Delta S_{H_2}^\circ$) are given in Figure 4 (standard errors for measured enthalpies and entropies are given as error bars) at each coverage for dispersed Pt particles with different mean diameters (1.6−9.1 nm). Even on large Pt particles (9.1 nm), $Q_{H_2}$ and $\Delta S_{H_2}^\circ$ values depend sensitively on H* coverage, in a manner indicative of H* binding that weakens and becomes more mobile as H*−H* distances decrease. These trends may reflect (i) repulsive H*−H* interactions, (ii) preferential occupancy of low-coordination surface sites at low coverages,[83] or (iii) adsorption on particles distributed in size and therefore in surface coordination (section 3.2). These coverage effects on $Q_{H_2}$ and $\Delta S_{H_2}^\circ$ values are discussed in more detail in sections 3.2 and 3.3.

**3.2. High-Temperature Adsorption Enthalpies.** The linear relations between $K_{H_2}$ values and reciprocal temperatures (Figure 3) indicate that the effects of temperature on the standard state heat of adsorption ($Q_{H_2}$) can be neglected over this relatively narrow temperature range (473−673 K).[89] The standard state heats of dissociative $H_2$ adsorption ($Q_{H_2}$) are 48−55 kJ mol-$H_2^{-1}$ at low coverages (~0.2 ML) and 40−46 kJ mol-$H_2^{-1}$ at 0.5 ML (Figure 4a) on these three samples (1.6−9.1 nm mean diameter); these thermodynamic properties correspond to those binding modes that prevail at 523−673 K, a temperature range characteristic of catalytic reactions involving $H_2$ and mediated by H* species. The heats of adsorption measured here (Figure 4a) are within the broad range of previously reported values (31−109 kJ mol$^{-1}$ at 0 ML and 21−92 kJ mol$^{-1}$ at 0.4−0.6 ML, Table 2). Our data and the literature values (Table 2) show general trends consistent with $Q_{H_2}$ values that are



DOI: 10.1021/acs.jpcc.8b10877
J. Phys. Chem. C 2019, 123, 8447−8462

**Table 2. Heat of $H_2$ Dissociative Adsorption on Pt Surfaces Reported in the Literature**

| surface | $Q_{H_2}$ (kJ mol$^{-1}$)[a] | coverage of H* ($\theta_H$) | $T$ (K) | method |
|---|---|---|---|---|
| Pt(100) | 96 | 0 | 78−300 | field emission probe-hole microscopy[36] |
| Pt(110) | 109 | 0 | 80−320 | field ion microscopy[38] |
| Pt(111) | 77 | 0 | 25−300 | thermal energy atom scattering and thermal desorption spectroscopy[39] |
| | 63 | 0.5 | | |
| Pt(111) | 94 | 0 | 90−240 | thermal energy atom scattering[40] |
| Pt(111) | 45 | 0 | 150−400 | work function change[41] |
| | 38 | 0.5 | | |
| | 29 | 0.8 | | |
| Pt(111) | 75 | 0 | 200−400 | low energy recoil scattering−isobars[42] |
| | 58 | 0.45 | | |
| stepped Pt(997) | 94 | 0 | 200−400 | low energy recoil scattering−isobars[42] |
| Pt black | 57 | 0 | 300 | calorimetry[43] |
| Pt filaments | 75 | 0.38 | 60−420 | adsorption isotherms[44] |
| | 46 | 0.46 | | |
| Pt filaments | 104 | 0 | 273 | UHV adiabatic calorimetric techniques[45] |
| | 92 | 0.5 | | |
| | 33 | 0.8 | | |
| Pt foil | 67 | 0 | 140−600 | adsorption isotherms[46] |
| | 21 | 0.5 | | |
| $Pt/Al_2O_3$ (1.1 nm)[b] | 61 | 0 | 300 | calorimetry[43] |
| $Pt/\eta$-$Al_2O_3$ (1.5 nm) | 62 | 0 | 215 | differential scanning calorimetry[47] |
| $Pt/SiO_2$ (15 nm) | 31 | 0 | 215 | differential scanning calorimetry[47] |
| $Pt/SiO_2$ (5.5 nm) | 69 | 0 | 300 | calorimetry[43] |
| $Pt/SiO_2$ (size n/a) | 84 | 0 | 308 | calorimetry[48] |

[a]Per mol of $H_2$; [b]Average Pt cluster size;

frequently lower at higher adsorption temperatures. $Q_{H_2}$ values at each coverage also decrease with increasing temperature because of the different heat capacities of $H_2$(g) and bound H*. Heat capacities for H*, derived from a degree-of-freedom analysis,[90,91] lead to an estimated decrease in heats of adsorption of <6 kJ mol$^{-1}$ between 300 and 673 K (Section S4; Supporting Information). These corrections are much smaller than the temperature effects of adsorption enthalpies evident from the data in Table 2, which therefore do not reflect such capacity corrections. H* can bind to an ensemble of equilibrated states some of which bind H* strongly (enthalpically) with little H* mobility and some which bind H* weakly (enthalpically) with greater H* mobility. The observed enthalpy changes would then reflect a gradual shift in the preferred H* binding modes, specifically toward weaker binding modes as temperature increases. This reflects a preference for H* states with higher entropy at higher temperatures to minimize adsorption free energies.

Standard state heats of adsorption ($Q_{H_2}$) decreased with increasing coverage on all Pt samples (1.6 nm; $Pt/SiO_2$; 3.0 and 9.1 nm; $Pt/Al_2O_3$) as a result of repulsive through-space or through-surface H*−H* interactions or surfaces that expose atoms of different coordination, with undercoordinated metal atoms that uptake H* strongly at low coverages and low-index planes that bind H* more weakly and become saturated at higher $H_2$ pressures (and H* coverages).

The initial decrease in $Q_{H_2}$ at low coverages (<0.3 ML, Figure 4a) is unlikely to reflect through-surface or through-space coadsorbate interactions at these low coverages (<0.2 ML for 1.6 nm; < 0.05 ML for 9.1 nm) and large H*−H* distances (>1.36 nm on average assuming a random distribution). Such a decrease in $Q_{H_2}$ values even below 0.3 ML appears to reflect H* species that predominantly occupy low-coordination edge and corner atoms at these low coverages,[3,92] leading to differential $Q_{H_2}$ values that then decrease as such sites reach saturation and H* incipiently populates low-index terraces with weaker binding. $Q_{H_2}$ values become nearly constant between 0.4−0.8 ML on 3.0 and 9.1 nm particles, indicative of negligible H*−H* coadsorbate interactions at these coverages. Undercoordinated sites are likely fully occupied by H* at these coverages and H* is likely binding to the Pt(111) surfaces which make up the majority of these particles (61% and 73% of similarly sized cuboctahedral particles).[83] Thus, these $Q_{H_2}$ values (40 and 35 kJ mol$^{-1}$) on 3.0 and 9.1 nm diameter particles for 0.4−0.8 ML likely reflect H* adsorption at these temperatures on Pt(111) surfaces.

Low-coordination atoms prevail at surfaces of small Pt particles (1.6 nm Pt cuboctahedral particles have 75% of all surface atoms in low-coordination environments),[83] consistent with higher heats of adsorption that are also less sensitive to H* coverage than on larger particles. The slight initial decrease in $Q_{H_2}$ values and the plateau observed between 0.4 and 0.8 ML on these 1.6 nm particles demonstrate that multiple under-coordinated sites exist (corners and distinct edges) which bind multiple H* with different strengths, as shown by DFT calculations on Ir and Pt particles,[3] indicating that site heterogeneity is present on small particles.

Standard state heats of adsorption ($Q_{H_2}$) values decrease sharply on all samples at $H_2$ pressures leading to H* coverages approaching 1 ML (Figure 4a). H* atoms interact repulsively at such coverages (>0.8 ML, mean H*−H* distances of 0.34 nm), as observed on Pt(111) surfaces in previous work.[3] Coverages greater than 1 ML become evident as $H_2$ pressures increase on all samples (Figure 2) even at 473 K and relatively low $H_2$ pressures (10 kPa), indicative of the expected prevalence of



DOI: 10.1021/acs.jpcc.8b10877
J. Phys. Chem. C 2019, 123, 8447−8462

Table 3. Adsorption Energies for H* on a 4 × 4 Pt(111) Surface at 593 K Using the RPBE Exchange-Correlation Functional[a]

| H* covg. | mode | $\Delta E_{0,H}$, kJ mol$^{-1}$ | $\Delta S_{vib,H}$, J mol$^{-1}$ K$^{-1}$ | $\Delta H_H$, kJ mol$^{-1}$ | $Q_{H_2}$,[b] kJ mol$^{-1}$ | $\Delta S_H$,[c] J mol$^{-1}$ K$^{-1}$ | $\Delta S_{H^*,conf}$, J mol$^{-1}$ K$^{-1}$ | $S_{H^*}$, J mol$^{-1}$ K$^{-1}$ | $\Delta G_H$, kJ mol$^{-1}$ | vibrational frequencies[d] cm$^{-1}$ | | |
|---|---|---|---|---|---|---|---|---|---|---|---|---|
| 0 → 1/16 | atop | −31 | 19 | −28 | 56 | −56 | 23 | 42 | −8 | 2262 | 369 | 368 |
| | fcc | −29 | 14 | −32 | 63 | −61 | 23 | 37 | −9 | 1086 | 593 | 588 |
| | hcp | −24 | 16 | −27 | 54 | −59 | 23 | 39 | −5 | 1102 | 524 | 523 |
| 7/16 → 1/2 | atop | −20 | 18 | −18 | 35 | −57 | 1 | 18 | 16 | 2254 | 431 | 371 |
| | fcc | −19 | 14 | −21 | 43 | −61 | 1 | 14 | 15 | 1099 | 742 | 551 |
| | hcp | −15 | 15 | −18 | 35 | −60 | 1 | 15 | 18 | 1105 | 585 | 498 |
| 15/16 → 1 | atop | −10 | 16 | −7 | 15 | −59 | −23 | −7 | 41 | 2241 | 451 | 450 |
| | fcc | −9 | 13 | −11 | 22 | −63 | −23 | −10 | 40 | 1164 | 651 | 649 |
| | hcp | −2 | 14 | −5 | 9 | −62 | −23 | −9 | 45 | 1162 | 610 | 607 |

[a]Table S4 in the Supporting Information shows other coverages, and Table S5 shows the same data using the PW-91 functional. [b]$Q_{H_2} = -2(\Delta H_H)$ [c]Gas-phase $H_2$ has $S_{trans}$ of 132 J mol$^{-1}$ K$^{-1}$ and $S_{rot}$ of 19 J mol$^{-1}$ K$^{-1}$. [d]Vibrational frequency of $H_2$(g) is 4331 cm$^{-1}$.

supramonolayer coverages during ambient $H_2$ chemisorption experiments typically used to determine metal dispersions, as reported previously on Pt/$Al_2O_3$ and Pt/$SiO_2$ (3 nm)[93−95] and confirmed by DFT-derived estimates of adsorption free energies on Pt nanoparticles (up to 586 atoms, 2.4 nm).[3]

The equilibrated nature of $H_2$ adsorption−desorption events during chemisorption measurements allows H* to bind to an ensemble of environments and reside in those environments with a probability distribution dictated by their relative free energies and the system temperature as described by Boltzmann. Adsorption enthalpies and entropies, therefore, are temperature-dependent over wide ranges (Table 2) leading to discrepancies between low-temperature studies (≤300 K) and high-temperature studies (≥450 K) and catalytic reactions. Adsorption enthalpies and entropies, furthermore, are dependent on the coverage and size of the metal particle as these two factors will influence the available ensemble of binding sites.

Next, we compare measured $Q_{H_2}$ values with those derived from DFT treatments of H* atoms present in distinct binding modes over a range of H* coverages (0−1 ML) on close-packed Pt(111) surfaces (Table 3) to probe whether this customary approach can describe the high-temperature adsorption data reported here. These close-packed Pt(111) planes prevail on large crystallites;[96] they contain three distinct H* binding locations: (i) atop (Figure 5a) with H* on top of a $Pt_{surf}$ atom; (ii) 3-fold fcc (Figure 5b); and (iii) 3-fold hcp (Figure 5c) sites, which differ in the presence (hcp) or absence (fcc) of a Pt atom in the immediate subsurface plane. DFT-derived $Q_{H_2}$ values differ slightly among these three sites at low coverages, with a slight preference for the fcc site (63 kJ mol$^{-1}$) over the atop (56 kJ mol$^{-1}$) and hcp (54 kJ mol$^{-1}$) sites (Table 3). $Q_{H_2}$ values on the Pt(111) surface decrease linearly by 41 kJ mol$^{-1}$ from 63 to 22 kJ mol$^{-1}$ (fcc-bound H*) as coverage increases from 1/16 to 1 ML (Figure 4a); similar decreases are evident for atop-bound H* (41 kJ mol$^{-1}$) and hcp-bound H* (45 kJ mol$^{-1}$).

Measured $Q_{H_2}$ values on 9.1 nm particles at 0.3−0.7 ML are essentially constant (35−37 kJ mol$^{-1}$) and they reflect the predominant contributions from the (111) terraces that prevail on large particles. DFT calculations, in contrast, predict $Q_{H_2}$ values that decrease linearly with coverage from 63 to 21 kJ mol$^{-1}$ as the Pt(111) surface is varied from 0 to 1 ML. Attractive van der Waals interactions among coadsorbed H* may compensate the repulsive effects described by the functionals used. These dispersive effects were then estimated using DFT-D3 methods (no H*−M interactions are included as H* is chemisorbed in these cases and therefore it will not have induced dipole interactions with the metal surface). These dispersive corrections did not influence DFT-derived $Q_{H_2}$ values at low coverage (1/16 ML), but increased $Q_{H_2}$ values at 1 ML from 21 to 32 kJ mol$^{-1}$, thus compensating for much of the H*−H* repulsion, but still preserving a monotonic decrease in $Q_{H_2}$ values with increasing H* coverage. It appears that the nearly constant $Q_{H_2}$ values observed between 0.3 and 0.7 ML H* reflect a slight expansion of the surface as H* coverage increases, as recently documented by DFT calculations of H* adsorption on Ir and Pt particles (38−586 atom clusters, 0.8−2.4 nm in diameter),[3] which would further mitigate H*−H* repulsion. PW-91 functionals typically "overbind",[97] thus leading to $Q_{H_2}$ values about 30 kJ mol$^{-1}$ larger than RPBE functionals at all coverages (Tables S3 and S4 in the Supporting Information). The effects of H* coverage on DFT-derived $Q_{H_2}$ values are, however, very similar when using these two functionals and they also decrease by ∼40 kJ mol$^{-1}$ as H* coverages increase from 1/16 to 1 ML using PW-91 functionals.

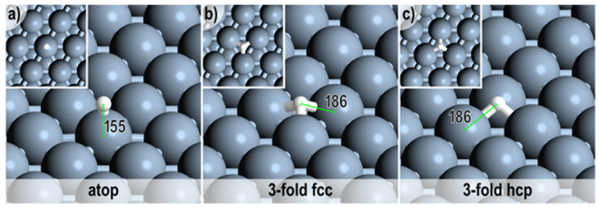


**Figure 5.** Binding modes and M−H bond lengths (in pm) for H* on a Pt(111) surface bound in (a) an atop mode to a single metal atom, (b) a 3-fold mode in an fcc hollow site, and (c) a 3-fold mode in an hcp hollow site. These specific bonding geometries were obtained at 1/16 ML H* on a 4 × 4 Pt(111) surface using the RPBE functional.

**3.3. Entropies of H* Species on Pt Surfaces.** Figure 4b shows the standard state entropy changes upon $H_2$ adsorption ($\Delta S_{H_2}$) on Pt particles (1.6−9.1 nm) at several H* coverages, measured from the temperature-dependent $K_{H_2}$ values at each coverage (Figure 3). These $\Delta S_{H_2}$ values (−20 to −80 J mol$^{-1}$ $H_2^{-1}$ K$^{-1}$; $\theta_H$ = 0.2−1.0; Figure 4b) reflect the loss of entropy per mol $H_2$(g) upon adsorption and the change in the entropy of



DOI: 10.1021/acs.jpcc.8b10877
J. Phys. Chem. C 2019, 123, 8447−8462

the H* adlayer upon adsorption of two additional H*, per mol $H_2$:

$$\Delta S_{H_2}(\theta_H) = 2\left(\frac{dS[H^*_{adlayer}]}{d\theta_H}\right) - S[H_2] \quad (26)$$

These $\Delta S_{H_2}$ can be combined with gas-phase $H_2$ entropies ($S[H_2]$) to calculate the change in adlayer entropy upon H* adsorption, which is defined here as the differential H* entropy ($S^*_H$), per mol H*:

$$S_{H^*} = \frac{dS[H^*_{adlayer}]}{d\theta_H} \quad (27)$$

Figure 6 shows differential molar H* entropies ($S_{H^*}$; per H atom) on Pt particles (1.6−9.1 nm mean diameter) as a function of H* coverage. Measured H* entropies decrease with increasing coverage on all samples (from 50−65 J $mol^{-1}$ $K^{-1}$ at 0.2 ML to 40−55 J $mol^{-1}$ $K^{-1}$ at 0.8 ML). Smaller particles give smaller $S_{H^*}$ values (by ~20 J $mol^{-1}$ $K^{-1}$ from 9.1 to 1.6 nm), consistent with the less mobile nature of the more strongly bound H* on smaller particles (Figure 4a). These H* entropies can be estimated using immobile and mobile models of the adsorbed species, as described below.

The entropies of H* species were calculated by treating H* as (I) an immobile adsorbate bound to specific binding sites, (II) an atom in an ideal two-dimensional gas, (III) an atom in a two-dimensional gas with an excluded area but without H*−H* interactions and (IV) an atom that samples a PES derived from DFT calculations, which rigorously includes interactions of H* with the Pt surface and coadsorbates.

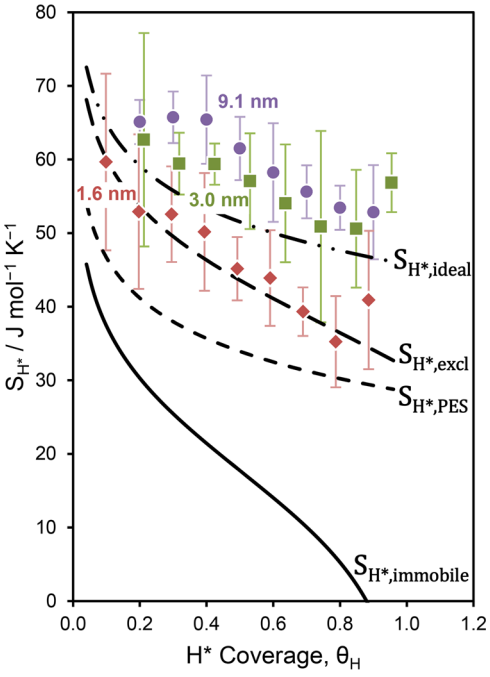


**Figure 6.** Entropy of H* on Pt as measured using $H_2$ isotherms on Pt particles with 9.1 nm (●, purple), 3.0 nm (■, green) and 1.6 nm (♦, red) mean cluster size and as estimated (at 598 K) for an immobile H* adsorbate with configurational contributions ($S_{H^*,immobile}$), an ideal mobile 2-D gas ($S_{H^*,ideal}$), a mobile 2-D gas with an excluded area term ($S_{H^*,excl}$), and a mobile H* sampling a PES ($S_{H^*,PES}$). Error bars represent standard errors from Arrhenius fits shown in Figure 3.

Differential H* entropies eq 28 for case I include the changes in configurational entropy caused by the addition of one more H* to the "checkerboard" ($S_{H^*,conf}$) and the entropy of the three vibrational degrees of freedom (two in-plane with the surface, one orthogonal to the surface) of an immobile H* adsorbate ($S^{xyz}_{H^*,vib}$):

$$S_{H^*,immobile} = S_{H^*,conf} + S^{xyz}_{H^*,vib} \quad (28)$$

H* bound in an atop position on Pt(111) surfaces has a DFT-derived vibrational frequency near 2250 $cm^{-1}$ (normal to the surface) and two vibrational modes near 400 $cm^{-1}$ along the surface plane, often denoted as "frustrated translations"; these vibrational frequencies vary slightly with coverage (Table 3). H* species at 3-fold sites have a normal vibrational mode near 1100 $cm^{-1}$ and two frustrated translations near 600 $cm^{-1}$ (Table 3). These frequencies lead to slightly larger $S_{H^*,vib}$ values at atop sites (19 J $mol^{-1}$ $K^{-1}$ at 593 K) than at either of the 3-fold location (fcc, 14 J $mol^{-1}$ $K^{-1}$; hcp, 16 J $mol^{-1}$ $K^{-1}$); $S_{H^*,vib}$ values differ by less than 5 J $mol^{-1}$ $K^{-1}$ from 0.06 to 1 ML (Table 3). An adlayer of immobile H* on a surface also has configurational entropy, as a system of $n$ adsorbates on $N$ sites in energetically equivalent configurations gives

$$S_{conf} = k_B \ln\left(\frac{N!}{n!(N-n)!}\right) \quad (29)$$

The differential configurational adsorption entropy can be determined from the derivative of eq 29 with respect to $n$:

$$S_{H^*,conf} = \frac{dS_{conf}}{dH^*} = -R \ln\left(\frac{\theta_H}{1-\theta_H}\right) \quad (30)$$

as previously derived.[98,99] These values, when combined with the vibrational entropies mentioned above, give $S_{H^*}$ values of 42 J $mol^{-1}$ $K^{-1}$ at H* coverages near 0 and −7 J $mol^{-1}$ $K^{-1}$ at H* coverages near 1 ML (Table 2) when H* atoms are bound in atop sites, with similar values (at both coverages) when H* atoms are bound in 3-fold sites (37 and 39 J $mol^{-1}$ $K^{-1}$ at low coverage and −10 and −9 J $mol^{-1}$ $K^{-1}$ at high coverage for fcc and hcp sites, respectively). These estimated $S_{H^*}$ values are much smaller than those measured (40−65 J $mol^{-1}$ $K^{-1}$, Figure 6) at all coverages, indicative of the significant mobility of H* on Pt particle surfaces at typical catalytic temperatures (473−673 K).

The H* adlayer can also be considered as an ideal two-dimensional gas (case II) with the differential entropy of a H* atom then given by

$$S_{H^*,ideal} = S^{xy}_{H^*,ideal} + S^{z}_{H^*,vib} \quad (31)$$

This model treats motion within the plane of the surface as two-dimensional translation ($S^{xy}_{H^*,ideal}$), and the remaining degree of freedom (motion normal to the surface) is treated as a vibration ($S^{z}_{H^*,vib}$), leading to a single vibration in the entropy estimates. The normal mode vibrational frequencies are ~2250 and 1100 $cm^{-1}$ at the atop and 3-fold binding locations on Pt(111) surfaces, respectively; consequently, they contribute less than 2 J $mol^{-1}$ $K^{-1}$ to the overall differential entropy values ($S_{H^*,ideal}$). An ideal two-dimensional gas model gives a uniform flat PES. The two-dimensional translational entropy of adsorbed H* ($S^{xy}_{H^*,ideal}$, eq 17) is the predominant contributor to $S_{H^*}$; it decreases as coverage increases, and this is analogous to the decrease in molar entropy with increasing pressure in a three-dimensional ideal gas.



DOI: 10.1021/acs.jpcc.8b10877
J. Phys. C 2019, 123, 8447−8462

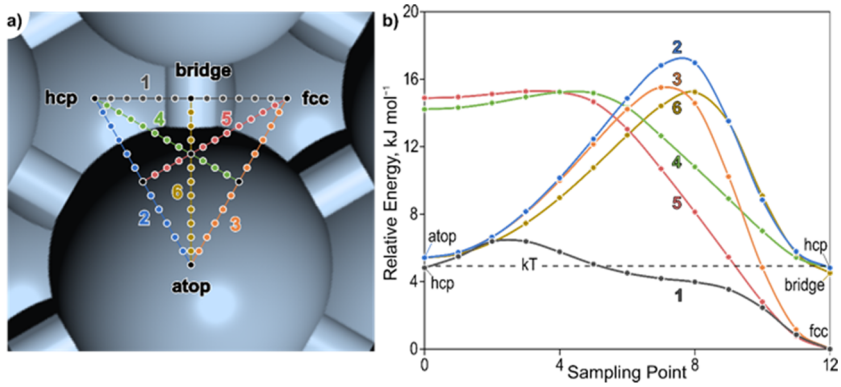


**Figure 7.** (a) Sampling of the Pt(111) surface for PES generation. (b) Relative energies (kJ mol$^{-1}$, RPBE) of each point for the six lines mapped out in part a. The thermal energy ($kT$) value is shown at 593 K.

In case III, the introduction of an "excluded area" term ($b$), to account for the area exclusion imposed by coadsorbed H* (eq 18) causes the translational entropy to decrease more sharply than the ideal case with increasing coverage (Figure 6).

Both the ideal ($S_{H^*,ideal}$) and the excluded area ($S_{H^*,co-area}$) H* adlayer models predict molar differential entropies ($S_{H^*}$) that decrease with increasing $\theta$, consistent with measured estimates; absolute values are also much closer to measured values than for the case of an immobile H* adlayer ($S_{H^*,immobile}$, Figure 6). This shows that H* species do not behave as immobile species at these temperatures; yet, some immobile species are required for Langmuirian treatments of adsorption and chemical reactions.

Thus far, we have described two extreme characterizations of H* mobility: immobile H* and barrierless H* diffusion. Next, we examine whether H* diffusion barriers are consistent with mobile species DFT-derived PES that include the barriers for diffusional H* hopping. These PES methods can be used to calculate a partition function and ultimately $S_{H^*}$ values. Coadsorbate interactions are rigorously captured through the modifications of the PES with increasing coverage. This PES treatment should give a larger $S_{H^*}$ value than the immobile H* model if the PES has anharmonic regions, and smaller $S_{H^*}$ than the ideal mobile H* model because H* binding energies vary with position on the Pt(111) surface (Table 3).

The Pt(111) surface was sampled at 67 points along 6 lines between the hcp, fcc, and atop sites using a H atom to generate the PES (Figure 7a). Potential energies ($E_0$) were combined with zero-point vibrational energies for modes normal to the surface ($ZPVE_z$) to account for the effects of the normal H* vibrations. The resulting energies (relative to the most stable binding mode, the 3-fold-fcc site) are shown in Figure 7b. This (111) surface, in contrast to the (100) surface previously modeled,[66] has multiple local minima (atop, 3-fold fcc and hcp sites) and three distinct diffusion pathways which interconnect these minima. This surface, therefore, is not amenable to a 2-dimensional sinusoidal treatment of the potential energies used in the hindered translator diffusion models presented elsewhere.[63−66] This motivates the use of the complete semiclassical treatment of the PES as described below. Diffusion from the fcc to the hcp site along sampling line 1 shows a 6 kJ mol$^{-1}$ barrier (RPBE, 1/16 ML H*, Figure 7b) which is just 30% larger than $kT$ at 593 K. These small fcc → hcp diffusion barriers (relative to $kT$) lead to anharmonic character, indicating that the harmonic oscillator approximation would be inaccurate for these entropy modes. Diffusion into and out of atop sites (sampling lines 2, 3, and 6), in contrast, show barriers of ~12 kJ mol$^{-1}$ (2.34 $kT$ at 593 K), indicative of activated H* diffusion. Rate coefficients for H* diffusion from and to atop sites were estimated to be on the order of $10^6$ s$^{-1}$ from these barriers and a pre-exponential factor of $10^7$ (on the low end of reported values).[100] Such high H* diffusion rates indicate that the H* adlayer is equilibrated within the 0.9−3.6 ks equilibration times used in the $H_2$ chemisorption measurements (Section 2). This indicates that H* atoms effectively sample all sites on the catalyst surface at each point in the isotherms and supports the assumptions of equilibrated $H_2$ adsorption/desorption and diffusion used throughout this work.

The energies, relative to the most energetically favorable binding mode, in Figure 7b are used to interpolate energies across the triangular region that lies between atop, hcp, and fcc sites (Figure 7a). The symmetry of the Pt(111) surface is then used to generate the PES for Pt(111) surfaces with unit cell sizes from 1 × 1 to 4 × 4, corresponding to 1/16 to 1 ML using the RPBE and PW-91 functionals (Figure 8). The low diffusional barriers connecting the 3-fold hcp and fcc sites create well-defined paths for rapid H* diffusion across the surface (marked in blue in Figure 8), consistent with mobile H* species which sample an ensemble of equilibrated states within the time scales of these isotherm measurements. These regions of low relative energy, along with those near the atop site, result in large areas that H* can occupy with similar probability. This leads to $S_{H^*}$ values derived from these PES sampling methods (eqs 16, Table 4) larger than those for immobile H* species, but lower than measured values (Figure 6).

As H* coverages increase and H*−H* distances decrease, the H* translational entropies decrease (as in the case of an ideal two-dimensional gas, eq 31), but the effective area per Pt atom ($\alpha_{PES}$) increases, because the PES becomes less "corrugated". At 0.06 ML, $\alpha_{PES}$ is 1.16 × 10$^{-2}$ nm$^2$, a value that corresponds to 17% of the area for the uniform PES (for a Pt atom in Pt(111) surfaces, 6.67 × 10$^{-2}$ nm$^2$) and $\alpha_{PES}$ increases to 1.99 × 10$^{-2}$ nm$^2$ (30%) at 1 ML. The higher H* coverages and the flatter PES combine to decrease $S_{H^*}$ values from 42 to 31 J mol$^{-1}$ K$^{-1}$ as the H* coverage increases from 0.2 to 0.8 ML (Figure 6); such trends are qualitatively consistent with the 10 J mol$^{-1}$ K$^{-1}$ decrease in measured $S_{H^*}$ values over a similar range of coverage. Immobile H* adsorption models, in contrast, predict a much larger decrease in $S_{H^*}$ values over this coverage range (~50 J mol$^{-1}$ K$^{-1}$, Figure 6) than all other models and much larger than the decrease in measured values (Figure 6). The PW-91 functional predicts larger barriers between atop and 3-fold sites (Figure 8b,d,f) than RPBE and predicts a less uniform PES with areas of higher relative energy than those observed using the



DOI: 10.1021/acs.jpcc.8b10877
J. Phys. Chem. C 2019, 123, 8447−8462

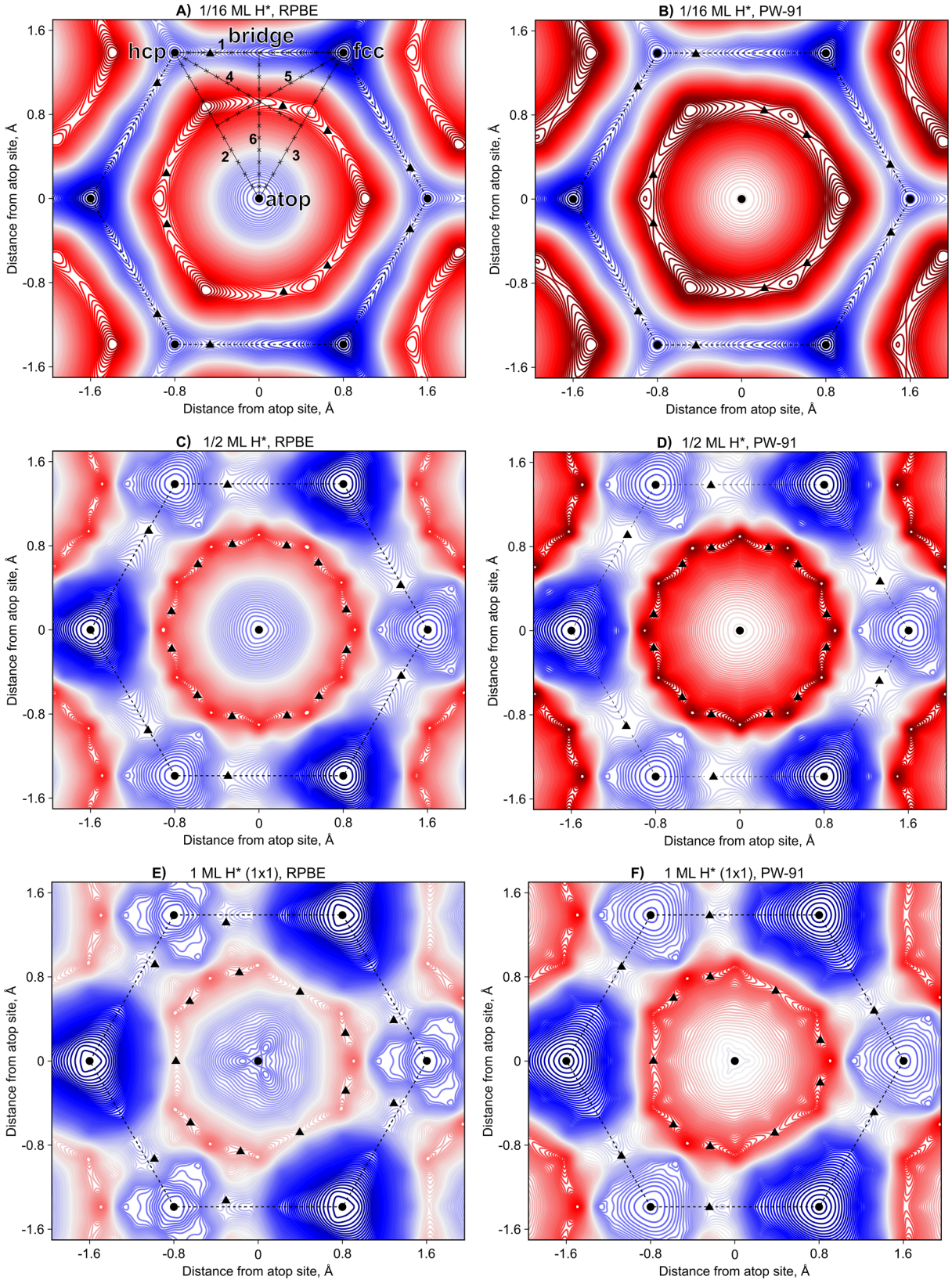


**Figure 8.** PES ($E_z$) for a H* atom on Pt(111) surfaces at (a) 1/16 ML (4 × 4, RPBE), (b) 1/16 ML (4 × 4, PW-91), (c) 1/2 ML (1 × 2, RPBE), (d) 1/2 ML (1 × 2, PW-91), (e) 1 ML (1 × 1, RPBE), and (f) 1 ML (1 × 1, PW-91). Symbols represent the following: (●) minima; (▲) saddle points (transition states for H* diffusion); (×) sampling points on the Pt(111) surface shown in part **a**. Line numbers correspond to Figure 7.

RPBE functional. These differences between the two functionals become more evident in surface regions where the energy is much larger than $kT$; these regions would be seldom sampled by diffusing H* species. Consequently, these differences between RPBE and PW-91 functionals do not affect $\alpha_{PES}$ at these temperatures. $S_{H^*}$ values decrease from 52 to 29 J mol$^{-1}$ K$^{-1}$ as



DOI: 10.1021/acs.jpcc.8b10877
J. Phys. Chem. C 2019, 123, 8447−8462

coverages increase from 0.06 to 1 ML using the PW-91-derived PES and from 52 to 30 J $mol^{-1}$ $K^{-1}$ for the RPBE-derived PES. These PES-derived $S_{H^*}$ values do not include any *ad hoc* assumptions about H* mobility; they treat the adlayer as one composed of noninteracting H* species that sample a PES imposed by the underlying Pt atoms, while H*−H* interactions are treated through the perturbations that they impose, in turn, on the PES. The $S_{H^*}$ values from this method lie between those for immobile H* (harmonic oscillator treatments of vibrational entropies and statistical mechanics formalisms for configurational entropies, eqs 28−30) and for H* atoms treated as a two-dimensional gas with or without excluded area terms, eqs 18 and 19.

Measured $S_{H^*}$ values are larger than those estimated from all these models of the H* adlayer (immobile, 2-D gas, PES; Figure 6), including the 2-D ideal gas treatments of the H* adlayer. Quantum-chemical treatments of PES have been previously compared to semiclassical treatments for H* on Pt(100) surfaces[66] and that work showed good agreement between the quantum and semiclassical treatments above ambient temperature, indicating that the deviations with experimental values would not be resolved by applying quantum methods. All treatments of these H* adlayers focus on the Pt(111) surface, which represents 45%, 61%, and 73% of cuboctahedral particles of 1.6, 3.0, and 9.1 nm in average diameter. If the models' underestimates of $S_{H^*}$ arose from the presence of (100) facets, corners, and edges, the discrepancies between model predictions and data would become more apparent on smaller particles, while the opposite trends are evident from the data in Figure 6. The diffusion of H* into subsurface regions of Pt particles may lead to lower $Q_{H_2}$ and higher $S_{H^*}$ values if the subsurface H* atoms are mobile within the crystallite bulk as they would be able to diffuse in three dimensions. The solubility of H atom in Pt metal, however, is very low;[101,102] in addition, H* migration into the bulk is endothermic by 45−75 kJ $mol^{-1}$ for $Pt_{79}$−$Pt_{405}$ atom particles (0.8−2.5 nm diameters),[3] indicating that subsurface H* are thermodynamically unfavorable, especially on larger particles, which show the largest deviation in $S_{H^*}$ between data and model predictions (Figure 6). PES-derived entropies eq 16 increase as the PES becomes more uniform or "flatter" (an ideal PES is completely flat). The strength of the H−M bond will directly impact adsorption enthalpies and the uniformity of the PES, as a stronger H−M bond will be more difficult to cleave during H*-diffusion events which would cause the diffusion barriers calculated here (Figure 7b) to increase and thus the PES would be more corrugated if DFT overestimates the H−M bond strength. This relationship between H−M bond strength and PES corrugation is also observed by comparing PES from the RPBE and PW-91 exchange correlation functionals (Figure 8), where the PW-91 functionals predict stronger H−M bonds (Table 3 and Table S5) and more corrugated PES. Thus, if DFT overpredicts H−M bond strength, as indicated by the overprediction in $H_2$ adsorption enthalpies (Figure 4a, RPBE, Table S5 for PW-91), it follows that DFT estimates of the PES are more corrugated than the true underlying PES, leading to underpredicted $S_{H^*}$ values from such estimates.

## 4. CONCLUSIONS

$H_2$ uptake measurements on Pt at moderate temperatures (523−673 K) have been used as a thermodynamic probe instead of a site-counting technique. These measurements on Pt particles (1.6−9.1 nm) gave adsorption entropies which indicate that chemisorbed hydrogen species are mobile and show that heats of adsorption decrease with increasing coverage. Thermodynamic properties of adsorption change with coverage in a manner consistent with the inherent nonuniformity of Pt particles that have exposed Pt sites with varying coordination and with mobile H* atoms that interact at high coverages. Statistical mechanics formalisms are used to estimate H* entropies from DFT-calculated vibrational frequencies and potential energy surfaces (PES) assuming (i) immobile H* and mobile H* on (ii) a uniform ideal PES, (iii) an area-excluded PES, and (iv) a DFT-derived PES. The mobile H* models estimate H* entropies that are significantly larger than the immobile H* model and within error of measured values. DFT-derived H* diffusion barriers, furthermore, are calculated to be within 1−2 kJ $mol^{-1}$ of thermal energies ($kT$) at these conditions (473−673 K), indicating that H* can rapidly diffuse between Pt-binding sites at these conditions. The high degree of mobility of H* and significant H*−H* interactions invalidate underlying assumptions within the ubiquitous Langmuir model. Yet, Langmuirian treatments are able to describe adsorption isotherms (including those presented in this work), indicating the insensitivity of individual isotherms to atomic properties. Langmuir models, therefore, merely provide a good phenomenological description of the process, and adsorption and kinetic parameters obtained from Langmuirian adsorption and kinetic models must be scrutinized in the context of adsorbate mobility and coadsorbate interactions, especially for species with relatively weak adsorbate-metal bonds. The nonideality of adsorbed hydrogen species, furthermore, also suggests that rigorous kinetic treatments for catalytic surface reactions should be based on activity and not on concentration and stresses the importance of gathering kinetic data over wide ranges of that activity and surface coverages.

## ■ ASSOCIATED CONTENT

### Supporting Information

The Supporting Information is available free of charge on the ACS Publications website at DOI: 10.1021/acs.jpcc.8b10877.

Derivations of thermodynamic treatments, local Langmuir isotherm adsorption models, alternative views of adsorption isotherms, frustrated translation treatment of diffusion, and details of DFT calculation results (PDF)

## ■ AUTHOR INFORMATION


### Corresponding Authors

*(D.D.H.) E-mail: hibbitts@che.ufl.edu.

*(E.I.) E-mail: iglesia@berkeley.edu.

### ORCID

David D. Hibbitts: 0000-0001-8606-7000

Enrique Iglesia: 0000-0003-4109-1001


### Notes

The authors declare no competing financial interest.

## ■ ACKNOWLEDGMENTS

This study has been funded by BP as part of the Methane Conversion Cooperative Research Program at the University of California at Berkeley. M.G.-D. acknowledges a postdoctoral fellowship from the Spanish Ministry of Science and Innovation (Mobility Grants for Postdoctoral Research). We thank Prof. David W. Flaherty for helpful technical discussions and providing the highly dispersed Pt sample. D.D.H. would like



DOI: 10.1021/acs.jpcc.8b10877
J. Phys. Chem. C 2019, 123, 8447−8462

to acknowledge Abdulrahman Almithn and Alexander Hoffman for editing and proofreading.

## REFERENCES

(1) Adamson, A. W. *Physical Chemistry of Surfaces*; 4th ed.; John Wiley & Sons, Inc.
(2) Cardona-Martinez, N.; Dumesic, J. A. Applications of Adsorption Microcalorimetry to the Study of Heterogeneous Catalysis. *Adv. Catal.* **1992**, *38*, 149−244.
(3) Almithn, A. S.; Hibbitts, D. D. Supra-monolayer Coverages on Small Metal Clusters and Their Effects on $H_2$ Chemisorption Particle Size Estimates. *AIChE J.* **2018**, *64*, 3109−3120.
(4) Dumesic, J. A.; Rudd, D. F.; Aparicio, L. M.; Rekoske, J. E.; Trevino, A. A. *The Microkinetics of Heterogeneous Catalysis*; ACS Professional Reference Book; American Chemical Society: Washington, DC, 1993.
(5) Bartholomew, C. H. *Catalysis − A Specialist Periodical Report*; The Royal Society of Chemistry: Cambridge, 1993, Vol. *11*, Chapter 3.
(6) Christmann, K. Interaction of Hydrogen with Solid Surfaces. *Surf. Sci. Rep.* **1988**, *9*, 1−163.
(7) Horiuti, I.; Polanyi, M. Exchange Reactions of Hydrogen on Metallic Catalysts. *Trans. Faraday Soc.* **1934**, *30*, 1164.
(8) Sinfelt, J. Catalytic Hydrogenolysis of Ethane over the Noble Metals of Group VIII. *J. Catal.* **1967**, *8*, 82−90.
(9) Davis, S. Deuterium Isotope Effects for Hydrocarbon Reactions Catalyzed over Platinum Single Crystal Surfaces. *J. Catal.* **1983**, *83*, 131−140.
(10) Flaherty, D. W.; Iglesia, E. Transition-state Enthalpy and Entropy Effects on Reactivity and Selectivity in Hydrogenolysis of N-alkanes. *J. Am. Chem. Soc.* **2013**, *135*, 18586−18599.
(11) Flaherty, D. W.; Hibbitts, D. D.; Gürbüz, E. I.; Iglesia, E. Theoretical and Kinetic Assessment of the Mechanism of Ethane Hydrogenolysis on Metal Surfaces Saturated with Chemisorbed Hydrogen. *J. Catal.* **2014**, *311*, 350−356.
(12) Flaherty, D. W.; Hibbitts, D. D.; Iglesia, E. Metal-catalyzed C-C Bond Cleavage in Alkanes: Effects of Methyl Substitution on Transition-state Structures and Stability. *J. Am. Chem. Soc.* **2014**, *136*, 9664−9676.
(13) Hibbitts, D. D.; Flaherty, D. W.; Iglesia, E. Role of Branching on the Rate and Mechanism of C−C Cleavage in Alkanes on Metal Surfaces. *ACS Catal.* **2016**, *6*, 469−482.
(14) Hibbitts, D. D.; Flaherty, D. W.; Iglesia, E. Effects of Chain Length on the Mechanism and Rates of Metal-catalyzed Hydrogenolysis of N-alkanes. *J. Phys. Chem. C* **2016**, *120*, 8125−8138.
(15) Almithn, A.; Hibbitts, D. Effects of Catalyst Model and High Adsorbate Coverages in Ab Initio Studies of Alkane Hydrogenolysis. *ACS Catal.* **2018**, *8*, 6375−6387.
(16) Goddard, S. Deuterium Tracing Studies and Microkinetic Analysis of Ethylene Hydrogenation over Platinum. *J. Catal.* **1992**, *137*, 186−198.
(17) Bond, G. C.; Wells, P. B. The Mechanism of the Hydrogenation of Unsaturated Hydrocarbons on Transition Metal Catalysts. *Adv. Catal.* **1965**, *15*, 91−226.
(18) Tsung, C.-K.; Kuhn, J. N.; Huang, W.; Aliaga, C.; Hung, L.-I.; Somorjai, G. A.; Yang, P. Sub-10 Nm Platinum Nanocrystals with Size and Shape Control: Catalytic Study for Ethylene and Pyrrole Hydrogenation. *J. Am. Chem. Soc.* **2009**, *131*, 5816−5822.
(19) Hibbitts, D. D.; Dybeck, E.; Lawlor, T.; Neurock, M.; Iglesia, E. Preferential Activation of CO Near Hydrocarbon Chains During Fischer−Tropsch Synthesis on Ru. *J. Catal.* **2016**, *337*, 91−101.
(20) Logan, M. Deuterium Isotope Effects on Hydrogenation of Carbon Monoxide over Rhodium. *J. Catal.* **1985**, *95*, 317−320.
(21) Loveless, B. T.; Buda, C.; Neurock, M.; Iglesia, E. CO Chemisorption and Dissociation at High Coverages During CO Hydrogenation on Ru Catalysts. *J. Am. Chem. Soc.* **2013**, *135*, 6107−6121.
(22) Liu, J.; Hibbitts, D.; Iglesia, E. Dense CO Adlayers as Enablers of CO Hydrogenation Turnovers on Ru Surfaces. *J. Am. Chem. Soc.* **2017**, *139*, 11789−11802.
(23) Vanmeerten, R. Isotope Effects in the Hydrogenation and Exchange of Benzene on Platinum and Nickel. *J. Catal.* **1979**, *58*, 43−51.
(24) Wang, H.; Iglesia, E. Thiophene Hydrodesulfurization Catalysis on Supported Ru Clusters: Mechanism and Site Requirements for Hydrogenation and Desulfurization Pathways. *J. Catal.* **2010**, *273*, 245−256.
(25) Wang, H.; Iglesia, E. Mechanism and Site Requirements of Thiophene Hydrodesulfurization Catalyzed by Supported Pt Clusters. *ChemCatChem* **2011**, *3*, 1166−1175.
(26) Hibbitts, D. D.; Jiménez, R.; Yoshimura, M.; Weiss, B.; Iglesia, E. Catalytic NO Activation and NO−$H_2$ Reaction Pathways. *J. Catal.* **2014**, *319*, 95−109.
(27) Nova, I.; Lietti, L.; Castoldi, L.; Tronconi, E.; Forzatti, P. New Insights in the $NO_x$ Reduction Mechanism with $H_2$ over Pt−Ba/$\gamma$-$Al_2O_3$ Lean $NO_x$ Trap Catalysts Under Near-isothermal Conditions. *J. Catal.* **2006**, *239*, 244−254.
(28) Boudart, M.; Djéga-Mariadassou, G. *Kinetics of Heterogeneous Catalytic Reactions*; Princeton University Press: Princeton, NJ, 2014.
(29) Piccinin, S.; Stamatakis, M. Steady-State CO Oxidation on Pd(111): First-Principles Kinetic Monte Carlo Simulations and Microkinetic Analysis. *Top. Catal.* **2017**, *60*, 141−151.
(30) Gao, F.; McClure, S. M.; Cai, Y.; Gath, K. K.; Wang, Y.; Chen, M. S.; Guo, Q. L.; Goodman, D. W. CO Oxidation Trends on Pt-group Metals from Ultrahigh Vacuum to Near Atmospheric Pressures: A Combined in Situ PM-IRAS and Reaction Kinetics Study. *Surf. Sci.* **2009**, *603*, 65−70.
(31) Allian, A. D.; Takanabe, K.; Fujdala, K. L.; Hao, X.; Truex, T. J.; Cai, J.; Buda, C.; Neurock, M.; Iglesia, E. Chemisorption of CO and Mechanism of CO Oxidation on Supported Platinum Nanoclusters. *J. Am. Chem. Soc.* **2011**, *133*, 4498−4517.
(32) Gürbüz, E. I.; Hibbitts, D. D.; Iglesia, E. Kinetic and Mechanistic Assessment of Alkanol/alkanal Decarbonylation and Deoxygenation Pathways on Metal Catalysts. *J. Am. Chem. Soc.* **2015**, *137*, 11984−11995.
(33) Zhuo, M.; Borgna, A.; Saeys, M. Effect of the CO Coverage on the Fischer−Tropsch Synthesis Mechanism on Cobalt Catalysts. *J. Catal.* **2013**, *297*, 217−226.
(34) Chin, Y.-H. C.; Buda, C.; Neurock, M.; Iglesia, E. Reactivity of Chemisorbed Oxygen Atoms and Their Catalytic Consequences During $CH_4$-$O_2$ Catalysis on Supported Pt Clusters. *J. Am. Chem. Soc.* **2011**, *133*, 15958−15978.
(35) Getman, R. B.; Schneider, W. F.; Smeltz, A. D.; Delgass, W. N.; Ribeiro, F. H. Oxygen-coverage Effects on Molecular Dissociations at a Pt Metal Surface. *Phys. Rev. Lett.* **2009**, *102*, 076101.
(36) Nieuwenhuys, B. E. Influence of the Surface Structure on the Adsorption of Hydrogen on Platinum, as Studied by Field Emission Probe-hole Microscopy. *Surf Sci* **1976**, *59*, 430−446.
(37) Gómez, R.; Orts, J. M.; Álvarez-Ruiz, B.; Feliu, J. M. Effect of Temperature on Hydrogen Adsorption on Pt(111), Pt(110), and Pt(100) Electrodes in 0.1 M $Hclo_4$. *J. Phys. Chem. B* **2004**, *108*, 228−238.
(38) Rootsaert, W. Field-emission Study of Composite Adsorption Layers on Tungsten and Platinum. *J. Catal.* **1962**, *1*, 416−431.
(39) Poelsema, B.; Lenz, K.; Comsa, G. The Dissociative Adsorption of Hydrogen on Defect-'free' Pt(111). *J. Phys.: Condens. Matter* **2010**, *22*, 304006.
(40) Poelsema, B.; Verheij, L. K.; Comsa, G. Temperature Dependency of the Initial Sticking Probability of $H_2$ and CO on Pt(111). *Surf. Sci.* **1985**, *152−153*, 496−504.
(41) Christmann, K.; Ertl, G.; Pignet, T. Adsorption of Hydrogen on a Pt(111) Surface. *Surf. Sci.* **1976**, *54*, 365−392.
(42) Koeleman, B. J. J.; de Zwart, S. T.; Boers, A. L.; Poelsema, B.; Verhey, L. K. Adsorption Study of Hydrogen on a Stepped Pt(997) Surface Using Low Energy Recoil Scattering. *Nucl. Instrum. Methods Phys. Res.* **1983**, *218*, 225−229.
(43) Sen, B.; Vannice, M. A. The Influence of Platinum Crystallite Size on $H_2$ and CO Heats of Adsorption and CO Hydrogenation. *J. Catal.* **1991**, *130*, 9−20.



DOI: 10.1021/acs.jpcc.8b10877
*J. Phys. Chem. C* 2019, 123, 8447−8462

(44) Norton, P. R.; Richards, P. J. The Heat of Adsorption of Hydrogen on Platinum. *Surf. Sci.* **1974**, *44*, 129−140.
(45) Norton, P. R.; Richards, P. J. Hydrogen Isotope Chemisorption and Equilibration on Platinum. *Surf. Sci.* **1974**, *41*, 293−311.
(46) Procop, M.; Völter, J. Adsorption von Wasserstoff an Platin. *Surf. Sci.* **1972**, *33*, 69−81.
(47) Vannice, M. Direct Measurements of Heats of Adsorption on Platinum Catalysts II. CO on Pt Dispersed on $SiO_2$, $Al_2O_3$, $SiO_2$-$Al_2O_3$, and $TiO_2$. *J. Catal.* **1986**, *97*, 66−74.
(48) Goddard, S. Kinetic Simulation of Heterogeneous Catalytic Processes: Ethane Hydrogenolysis over Supported Group VIII Metals. *J. Catal.* **1989**, *117*, 155−169.
(49) Bond, G. C. *Metal-Catalysed Reactions of Hydrocarbons*; Springer: New York, 2005.
(50) Feibelman, P. J.; Hamann, D. R. Theory of H Bonding and Vibration on Pt(111). *Surf. Sci.* **1987**, *182*, 411−422.
(51) Feibelman, P. J. First-principles Calculations of Stress Induced by Gas Adsorption on Pt(111). *Phys. Rev. B: Condens. Matter Mater. Phys.* **1997**, *56*, 2175−2182.
(52) Olsen, R. A.; Kroes, G. J.; Baerends, E. J. Atomic and Molecular Hydrogen Interacting with Pt(111). *J. Chem. Phys.* **1999**, *111*, 11155−11163.
(53) Watson, G. W.; Wells, R. P. K.; Willock, D. J.; Hutchings, G. J. Ab Initio Simulation of the Interaction of Hydrogen with the {111} Surfaces of Platinum, Palladium and Nickel. A Possible Explanation for Their Difference in Hydrogenation Activity. *Chem. Commun.* **2000**, 705−706.
(54) Papoian, G.; Nørskov, J. K.; Hoffmann, R. A Comparative Theoretical Study of the Hydrogen, Methyl, and Ethyl Chemisorption on the Pt(111) Surface. *J. Am. Chem. Soc.* **2000**, *122*, 4129−4144.
(55) Bădescu, S. C.; Salo, P.; Ala-Nissila, T.; Ying, S. C.; Jacobi, K.; Wang, Y.; Bedürftig, K.; Ertl, G. Energetics and Vibrational States for Hydrogen on Pt(111). *Phys. Rev. Lett.* **2002**, *88*, 136101.
(56) Pijper, E.; Kroes, G. J.; Olsen, R. A.; Baerends, E. J. Reactive and Diffractive Scattering of $H_2$ from Pt(111) Studied Using a Six-dimensional Wave Packet Method. *J. Chem. Phys.* **2002**, *117*, 5885−5898.
(57) Hammer, B.; Norskov, J. K. Why Gold Is the Noblest of All the Metals. *Nature* **1995**, *376*, 238−240.
(58) Paz-Borbon, L. O.; Johnston, R. L.; Barcaro, G.; Fortunelli, A. Chemisorption of CO and H on Pd, Pt and Au Nanoclusters: a DFT Approach. *Eur. Phys. J. D* **2009**, *52*, 131−134.
(59) Zhou, C.; Wu, J.; Nie, A.; Forrey, R. C.; Tachibana, A.; Cheng, H. On the Sequential Hydrogen Dissociative Chemisorption on Small Platinum Clusters: A Density Functional Theory Study. *J. Phys. Chem. C* **2007**, *111*, 12773−12778.
(60) Chen, L.; Cooper, A. C.; Pez, G. P.; Cheng, H. Density Functional Study of Sequential $H_2$ Dissociative Chemisorption on a $Pt_6$ Cluster. *J. Phys. Chem. C* **2007**, *111*, 5514−5519.
(61) Okamoto, Y. Comparison of Hydrogen Atom Adsorption on Pt Clusters with That on Pt Surfaces: A Study from Density-functional Calculations. *Chem. Phys. Lett.* **2006**, *429*, 209−213.
(62) Ferrin, P.; Kandoi, S.; Nilekar, A. U.; Mavrikakis, M. Hydrogen Adsorption, Absorption and Diffusion on and in Transition Metal Surfaces: A DFT Study. *Surf. Sci.* **2012**, *606*, 679−689.
(63) Campbell, C. T.; Sellers, J. R. V. The Entropies of Adsorbed Molecules. *J. Am. Chem. Soc.* **2012**, *134*, 18109−18115.
(64) Sprowl, L. H.; Campbell, C. T.; Árnadóttir, L. Hindered Translator and Hindered Rotor Models for Adsorbates: Partition Functions and Entropies. *J. Phys. Chem. C* **2016**, *120*, 9719−9731.
(65) Campbell, C. T.; Sprowl, L. H.; Árnadóttir, L. Equilibrium Constants and Rate Constants for Adsorbates: Two-Dimensional (2D) Ideal Gas, 2D Ideal Lattice Gas, and Ideal Hindered Translator Models. *J. Phys. Chem. C* **2016**, *120*, 10283−10297.
(66) Bajpai, A.; Mehta, P.; Frey, K.; Lehmer, A. M.; Schneider, W. F. Benchmark First-Principles Calculations of Adsorbate Free Energies. *ACS Catal.* **2018**, *8*, 1945−1954.
(67) Jørgensen, M.; Grönbeck, H. Adsorbate Entropies with Complete Potential Energy Sampling in Microkinetic Modeling. *J. Phys. Chem. C* **2017**, *121*, 7199−7207.
(68) Miller, J. A. Fundamental Study of Platinum Tetraammine Impregnation of Silica2. The Effect of Method of Preparation, Loading, and Calcination Temperature on (reduced) Particle Size. *J. Catal.* **2004**, *225*, 203−212.
(69) Schneider, M.; et al. High Surface Area Platinum-Titania Aerogels: Preparation, Structural Properties, and Hydrogenation Activity. *J. Catal.* **1994**, *147*, 500−514.
(70) Gilbert, R. G.; Hess, M.; Jenkins, A. D.; Jones, R. G.; Kratochvil, P.; Stepto, R. F. T. Dispersity in Polymer Science (IUPAC Recommendations 2009). *Pure Appl. Chem.* **2009**, *81*, 351−353.
(71) Kresse, G.; Hafner, J. *Ab Initio* Molecular Dynamics for Liquid Metals. *Phys. Rev. B: Condens. Matter Mater. Phys.* **1993**, *47*, 558−561.
(72) Kresse, G.; Hafner, J. Ab Initio Molecular-dynamics Simulation of the Liquid-metal-amorphous-semiconductor Transition in Germanium. *Phys. Rev. B: Condens. Matter Mater. Phys.* **1994**, *49*, 14251−14269.
(73) Kresse, G.; Furthmüller, J. Efficiency of Ab-initio Total Energy Calculations for Metals and Semiconductors Using a Plane-wave Basis Set. *Comput. Mater. Sci.* **1996**, *6*, 15−50.
(74) Kresse, G.; Furthmüller, J. Efficient Iterative Schemes For *Ab Initio* Total-energy Calculations Using a Plane-wave Basis Set. *Phys. Rev. B: Condens. Matter Mater. Phys.* **1996**, *54*, 11169−11186.
(75) Blöchl, P. E. Projector Augmented-wave Method. *Phys. Rev. B: Condens. Matter Mater. Phys.* **1994**, *50*, 17953−17979.
(76) Kresse, G.; Joubert, D. From Ultrasoft Pseudopotentials to the Projector Augmented-wave Method. *Phys. Rev. B: Condens. Matter Mater. Phys.* **1999**, *59*, 1758−1775.
(77) Perdew, J. P.; Burke, K.; Ernzerhof, M. Generalized Gradient Approximation Made Simple. *Phys. Rev. Lett.* **1996**, *77*, 3865−3868.
(78) Zhang, Y.; Yang, W. Comment on "Generalized Gradient Approximation Made Simple. *Phys. Rev. Lett.* **1998**, *80*, 890−890a.
(79) Hammer, B.; Hansen, L. B.; Nørskov, J. K. Improved Adsorption Energetics Within Density-functional Theory Using Revised Perdew-Burke-Ernzerhof Functionals. *Phys. Rev. B: Condens. Matter Mater. Phys.* **1999**, *59*, 7413−7421.
(80) Perdew, J. P.; Chevary, J. A.; Vosko, S. H.; Jackson, K. A.; Pederson, M. R.; Singh, D. J.; Fiolhais, C. Atoms, Molecules, Solids, and Surfaces: Applications of the Generalized Gradient Approximation for Exchange and Correlation. *Phys. Rev. B: Condens. Matter Mater. Phys.* **1992**, *46*, 6671−6687.
(81) Grimme, S.; Antony, J.; Ehrlich, S.; Krieg, H. A Consistent and Accurate Ab Initio Parametrization of Density Functional Dispersion Correction (DFT-D) for the 94 Elements H-Pu. *J. Chem. Phys.* **2010**, *132*, 154104.
(82) Grimme, S.; Ehrlich, S.; Goerigk, L. Effect of the Damping Function in Dispersion Corrected Density Functional Theory. *J. Comput. Chem.* **2011**, *32*, 1456−1465.
(83) Van Hardeveld, R.; Hartog, F. The Statistics of Surface Atoms and Surface Sites on Metal Crystals. *Surf. Sci.* **1969**, *15*, 189−230.
(84) Lonsdale, K.; MacGillavry, C. H.; Rieck, G. D.; Crystallography., I. U. of. *International Tables for X-ray Crystallography*, Vol. III; Published for the International Union of Crystallography by D. Reidel Pub. Co.: Dordrecht, The Netherlands, and Boston, MA, 1985.
(85) McQuarrie, D. A. *Statistical Mechanics*; University Science Books: Sausalito, CA, 2000.
(86) Shell, M. S. *Thermodynamics and Statistical Mechanics: An Integrated Approach*; Cambridge University Press: 2015.
(87) Clark, A. *The Theory of Adsorption and Catalysis*; Academic Press: 1970; Vol. *18*.
(88) Singh, K. S. W.; Rouquerol, J.; Bergeret, G.; Gallezot, P.; Vaarkamp, M.; Koningsberger, D. C.; Datye, A. K.; Niemantsverdriet, J. W.; Butz, T.; Engelhardt, G. Characterization of Solid Catalysts: Sections 3.1.1− 3.1.3. *Handbook of heterogeneous catalysis* **1997**, 427−582.



DOI: 10.1021/acs.jpcc.8b10877
J. Phys. Chem. C 2019, 123, 8447−8462

(89) Shen, D.; Bülow, M.; Siperstein, F.; Engelhard, M.; Myers, A. L. Comparison of Experimental Techniques for Measuring Isosteric Heat of Adsorption. *Adsorption* **2000**, *6*, 275−286.
(90) Huang, Y. The Temperature Dependence of Isosteric Heat of Adsorption on the Heterogeneous Surface. *J. Catal.* **1972**, *25*, 131−138.
(91) Al-Muhtaseb, S. A.; Ritter, J. A. A Statistical Mechanical Perspective on the Temperature Dependence of the Isosteric Heat of Adsorption and Adsorbed Phase Heat Capacity. *J. Phys. Chem. B* **1999**, *103*, 8104−8115.
(92) Winkler, A.; Guo, X.; Siddiqui, H. R.; Hagans, P. L.; Yates, J. T. Kinetics and Energetics of Oxygen Adsorption on Pt(111) and Pt(112)- A Comparison of Flat and Stepped Surfaces. *Surf. Sci.* **1988**, *201*, 419−443.
(93) Kip, B. Determination of Metal Particle Size of Highly Dispersed Rh, Ir, and Pt Catalysts by Hydrogen Chemisorption and EXAFS. *J. Catal.* **1987**, *105*, 26−38.
(94) Sato, S. Photoelectrochemical Preparation of $Pt/TiO_2$ Catalysts. *J. Catal.* **1985**, *92*, 11−16.
(95) Kip, B. J.; Duivenvoorden, F. B. M.; Koningsberger, D. C.; Prins, R. Determination of Metal Particle Size of Highly Dispersed Rhodium, Iridium and Platinum Catalysts by Hydrogen Chemisorption and EXAFS. *J. Am. Chem. Soc.* **1986**, *108*, 5633−5634.
(96) Skriver, H. L.; Rosengaard, N. M. Surface Energy and Work Function of Elemental Metals. *Phys. Rev. B: Condens. Matter Mater. Phys.* **1992**, *46*, 7157−7168.
(97) Wellendorff, J.; Silbaugh, T. L.; Garcia-Pintos, D.; Nørskov, J. K.; Bligaard, T.; Studt, F.; Campbell, C. T. A Benchmark Database for Adsorption Bond Energies to Transition Metal Surfaces and Comparison to Selected DFT Functionals. *Surf. Sci.* **2015**, *640*, 36−44.
(98) Everett, D. H. The Thermodynamics of Adsorption. Part II.—Thermodynamics of Monolayers on Solids. *Trans. Faraday Soc.* **1950**, *46*, 942−957.
(99) Denbigh, K. G. *The principles of chemical equilibrium: with applications in chemistry and chemical engineering*; Cambridge University Press: 1981.
(100) Baetzold, R. Preexponential Factors in Surface Reactions. *J. Catal.* **1976**, *45*, 94−105.
(101) McLellan, R. B.; Oates, W. A. The Solubility of Hydrogen in Rhodium, Ruthenium, Iridium and Nickel. *Acta Metall.* **1973**, *21*, 181−185.
(102) Katsuta, H.; McLellan, R. B. Diffusivity Permeability and Solubility of Hydrogen in Platinum. *J. Phys. Chem. Solids* **1979**, *40*, 697−699.



DOI: 10.1021/acs.jpcc.8b10877
*J. Phys. Chem. C* 2019, 123, 8447−8462